Justus-Liebig-Universität Gießen
Physikalisch-Chemisches Institut

Università degli Studi di Padova
Dipartimento di Scienze Chimiche

DOUBLE DEGREE PROGRAM

MASTER'S DEGREE IN CHEMISTRY

FeS_2-Based Na–S Solid-State Batteries: Impact of Positive Electrode Microstructure and Additives on Cell Performance

Marta Rando

Thesis Supervisors:

Prof. Dr. J. Janek

Prof. Dr. A. Henss

Prof. Dr. C. Durante

Academic Year 2024/2025

Contents

Abstract

Pyrite-based sodium-sulfur (Na-S) solid-state batteries (SSBs) are considered as the next generation of sustainable energy storage systems because of the use of highly abundant materials, the expected high energy and power densities, and the improved capacity. However, until now FeS_2-based Na-S solid state batteries have not received much attention because of the difficulty in finding suitable solid electrolytes (SEs). Furthermore, research on Na solid-state batteries is in its early stages. Driven by the advantages of using both FeS_2 and Na in a solid-state battery, this work focuses on the investigation of an all-solid-state cell setup with a composite cathode made of FeS_2 (cathode active material), Na_3PS_4, and carbon black, Na_3PS_4 as the separator, and a sodium tin alloy as the anode. In particular, the positive electrode microstructure and the effect of an additive (NaI) were examined using electrochemical and analytical methods, such as galvanostatic charge-discharge (GCD) and scanning electron microscopy (SEM). Our results show that smaller particle size within the composites is key for allowing active material utilization and achieving high capacities.

Although the redox-mediating effect of NaI remains unclear, studies performed on Li-S systems suggest that iodine is effective in enhancing fast charging capabilities for solid-state batteries. For this reason, further investigation on the topic is needed.

1 Introduction

As the world's energy crisis advances, strategies to reduce fossil fuel consumption are highly needed. In this context, secondary batteries play a key role in enabling the effective utilization of renewable energies [1]. Among the different battery technologies, lithium-sulfur batteries (Li-S) are promising because they are expected to have high energy densities (up to 2600 Wh kg^{-1}) and theoretical gravimetric capacities (1675 mAh g^{-1}). Further, sulfur is a low-cost, earth-abundant element [2, 3]. However, the utilization of Li-S batteries is restrained by four main issues. First, the use of a lithium metal anode often causes electrolyte degradation and dendrite formation, which might cause short circuits and introduce safety issues such as heat accumulation and gas evolution. Second, sulfur and its discharging and charging products are both electronic and ionic insulators. This brings about kinetic difficulties that can be overcome only by integrating large amounts of ionic and electronically conductive additives inside the cathode. In addition, considerable volume change is expected during cycling and can cause cracking and loss of cathode active material. Lastly, the polysulfide shuttle effect is one of the main causes of cell failure. In fact, in Li-S cells, different polysulfides (PS) species that can dissolve in liquid electrolytes are formed during cycling. PS can then shuttle back and forth between the electrodes and cause coulombic inefficiency, corrosion of the anode, and failure [2, 3, 4]. To overcome the main challenges of Li-S batteries, many strategies can be employed. For example, metal sulfides that show better electronic conductivities compared to sulfur can be used as cathode active materials (CAMs) [5]. As an example, CuS, NiS_2, CoS_2 and FeS_2 are attractive as active materials due to their low cost [6, 7]. Among the sulfides, pyrite (FeS_2) stands out as cathode active material because of its earth abundance (largest reserve of sulfide minerals in the earth's crust), cheap price, non-toxicity and high theoretical capacity (894 mAh g^{-1}) enabled by its four-electron redox process (Eq. 1).

$$FeS_2 + 4Na^+ + 4e^- \rightarrow FeS + 2Na_2S \quad (1)$$

Moreover, with its semiconductor properties, pyrite is especially suitable for optoelectronic and battery applications [8, 9, 10].

In any case, pyrite-based Li-S batteries still face issues such as polysulfide shuttle, volume expansion, and dendrite formation. A possible strategy to overcome the problem of PS shuttle is to use an all-solid-state cell setup [5, 11]. In solid-state batteries (SSBs) liquid electrolytes are replaced with solid electrolytes (SEs). This brings significant advantages and paves the way for new opportunities; however, SSBs also come with a number of challenges. The most important benefits of using solid state batteries come from the possibility of achieving improved energy and power densities, avoiding shuttling effects, and having better stability at elevated temperatures. Moreover, the use of oxide ceramic solid electrolytes improves battery safety since they are stable against lithium and are not combustible (unlike liquid electrolytes), but this is not true for sulfide electrolytes that face safety issues related to the formation of toxic H_2S [11]. Figure 1 shows a schematic representation of the difference between Li-S and Li-S solid-state batteries.

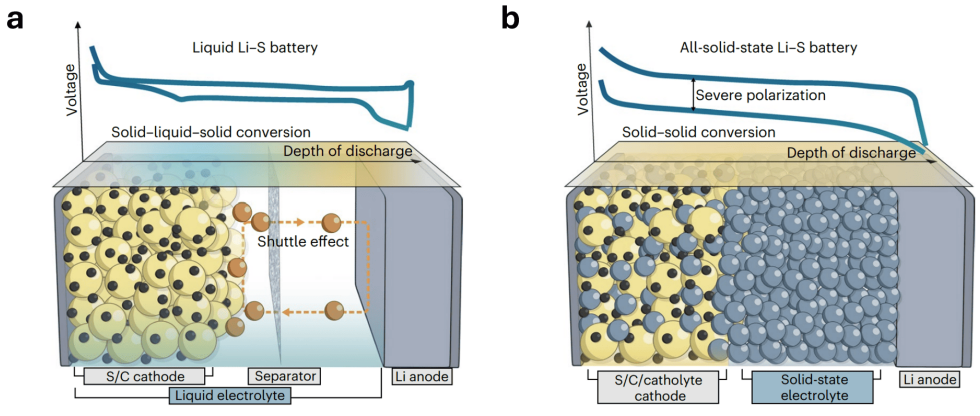

Figure 1: a) Voltage profile, conversion mechanism and battery architecture of a typical liquid Li–S battery b) and a typical all-solid-state Li–S battery. The choice of electrolyte chemistry and its phase (liquid or solid) influences the electrochemical behavior of the cell. In particular, the number of plateaus present in the voltage profiles and the overpotential are different for Li-S and Li-S SSBs [12].

On the other hand, the main challenges are volume changes (159 % of volume expansion for FeS_2), particle cracking, sluggish kinetics, and, regarding the anode side, filament and dendrite formation [11, 13]. In particular, some of the most critical challenges for both Li-S and pyrite-based Li-S SSBs concern volume expansions and the insulating nature of the active materials and the products formed during cycling [14]. In Li-S batteries volume expansion is particularly critical since both S and FeS_2 are conversion materials which during lithiation / delithiation undergo structural rearrangements to form different chemical species [7, 5]. In addition, to improve ionic and electronic conductivities, large amounts of solid electrolytes and electron-conductive additives (e.g. carbon) have to be included inside the positive electrodes. In this case, electrochemical reactions will occur at the triple phase boundary between SE, CAM, and the electron-conductive additive, which makes microstructure and fast ionic transport within the composite exceptionally important [13]. To establish sufficient triple-phase boundaries a large contact area between the cathode components is required; nevertheless, this promotes the degradation of the solid electrolytes and may cause cell failure[14].

One of the major challenges of Li-S batteries is the availability of lithium in the earth's crust. As a matter of fact, lithium is considered a critical raw material, meaning that there is increasing concern regarding its supply disruption [15]. This would make lithium batteries unsuitable for stationary applications, for which the most important parameters are price (therefore the need of abundant materials), life, and power [16]. Sodium is considered one of the most promising alternatives to lithium because of its abundance and its chemical properties similar to lithium [17, 18, 19]. Figure 2 shows the availability and distribution of Li in the earth's crust, while global Na reservoirs can be considered infinite [16].

As a consequence, Na-S solid-state batteries are considered the next generation of sustainable energy systems because of the abundance of both sodium and sulfur, and their high expected energy densities and improved cycling stability and capacity. Unfortunately, major obstacles such as ir-

Figure 2: "Global distribution of identified Li resources at the end of 2019. The amounts in each location are proportional to the areas of the circles shown. All locations with at least one million tons are indicated; together, they make up 97% of the global total". [20]

reversible sulfur conversion, interface issues, and sluggish solid-solid redox kinetics need to be faced. Additionally, the low ionic conductivity and poor compatibility of the solid electrolytes with the electrodes still hinder the effective use of Na-S solid state batteries [21, 22]. In fact, there is still no solid electrolyte for sodium batteries that meets the requirements of good ionic conductivity, sufficient interfacial contact, stability, feasibility to integrate with electrodes and manufacture cost. Particularly, one of the main challenges of these electrolytes is the narrow electrochemical stability window and compatibility to high capacity/ voltage electrodes (for example Na metal). The most promising electrolytes for Na SSBs are $Na_2B_nH_n$ and $NaCB_{n-1}H_n$ solid electrolytes because of their high conductivity, interfacial integration and stability. However, their high cost remains a critical drawback [23, 24]. In this work, a sulfide elctrolyte (Na_3PS_4) is employed as the separator, despite of its chemical and electrochemical stability [25]. In fact, sulfide electrolytes are particularly suitable for pyrite-based solid-state batteries because of their compatibility and chemical stability with FeS_2 [26]. In addition, they are able to establish intimate contact with the electrodes due to their softness and deformability [24].

Among the various challenges of SSBs, fast charging (15 minutes of recharge time) remains critical. In fact, although different attempts have been made to achieve fast charging, such as the use of coatings and additives, research is still ongoing [27]. Indeed, at the battery level, there are still crucial challenges that need to be addressed. Specifically, insufficient active material utilization, excessive heat generation, increased propensity to dendrite growth, and presence of new degradation mechanisms are the main issues that limit fast charging capabilities [27].

In this regard, Song *et al.* developed an all-solid-state lithium sulfur battery setup that shows ultrafast charging capabilities (the cells maintain 784 mAh $g^{-1}{}_{sulfur}$ at 20C) [28]. This was achieved using lithium thioborophosphate iodide glass phase solid electrolytes (LBPSI) that show high conductivities and act as surfacial redox mediators that facilitate sluggish solid-solid reactions [28]. In fact, it was demonstrated that iodine (I_2 / I_3^-) acts as surfacial redox mediator that facilitates the oxidation of Li_2S (which is electronically insulating) at the SE |C boundary during charge. This process has the advantage of enabling the reaction at the two-phase boundary between SE and Li_2S which would otherwise be inactive (Figure 3) [28].

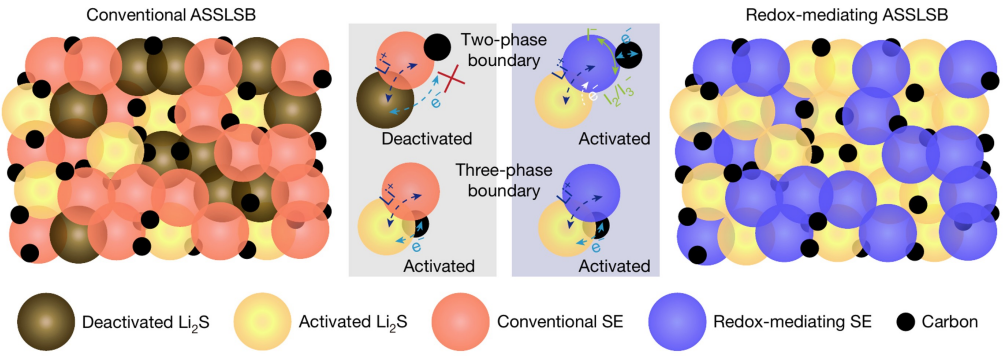

Figure 3: "Schematic showing the design principle for the fast-charging mechanism of ASSLSBs. The redox-mediating SE shown in blue is moderately redox active and generates surficial I_2/I_3^- to mediate the sulfur reaction on fast charge; this revitalizes reactions at the SE|active material two-phase boundary that is otherwise inactive and much more populated than the conventionally required SE|C|active material three-phase boundary". Adapted from [28].

The redox mediating role of iodine (LBPSI) based on the reversible reaction between I^- and I_2 / I_3^- during charge can be summarized by the following proposed reactions [28].

1. Oxidation of LBPSI to form surfacial I^-

2. Mediated chemical oxidation of Li_2S at the two phase boundaries

$$Li_2S + I_2 \rightarrow S + 2Li^+ + 2I^- \tag{2}$$

$$Li_2S + I_3^- \rightarrow S + 2Li^+ + 3I^- \tag{3}$$

3. Electrochemical oxidation of Li_2S at the three phase boundary

$$Li_2S - 2e^- \rightarrow S + 2Li^+ \tag{4}$$

Motivated by the question of whether the strategies that have proven effective in overcoming the intrinsic challenges of Li–S solid-state batteries can also be applied to sodium systems, this work focuses on a pyrite-based Na–S solid cell setup.

Inspired by the work of Song *et. al*, the effect of sodium iodide (NaI) as an additive inside the positive electrode will be discussed. NaI was chosen as additive because of the ease of integrating it inside cathode composites. The setup under investigation is composed of a composite cathode containing FeS_2, Na_3PS_4, and carbon black, Na_3PS_4 as solid electrolyte and Na-Sn as the anode. However, because of the novelty of this system (very few already published works and only in the last years), research on the single cell components was carried out. In particular, the stability of the negative electrode and the influence of the positive electrode microstructure on the cell performance were investigated. To do this, electrochemical analysis was employed in combination with analytical tests. For example, galvanostatic charge-discharge (GCD) and electrochemical impedance spectroscopy (EIS) were used to assess the performance of the cell setup and examine interface stability. X-ray diffraction (XRD) and scanning electron microscopy (SEM)

were used to investigate the structure of the cathode composites, and X-ray photoelectron spectroscopy (XPS) was employed to study the reactions at the positive electrode.

2 Theoretical background

There are many suitable techniques for understanding the complex processes that occur inside a battery. Usually, to study battery operation, a synergy of electrochemical and analytical techniques is needed. Among the different electrochemical methods, cyclic voltammetry (CV), galvanostatic charge-discharge methods (GCD), galvanostatic intermittent titration techniques (GITT), and electrochemical impedance spectroscopy (EIS) stand out [29]. In fact, these techniques provide valuable information on the capacity, reversibility, stability, and rate capability of electrode materials. Additionally, they allow the study of diffusion coefficients and interface stability. However, most of the time these methods alone are not sufficient to understand the intricate processes that are taking place inside batteries. For this reason, analytical techniques such as X-ray diffraction (XRD), Scanning electron microscopy (SEM), Transmission electron microscopy (TEM), and X-ray photoelectron spectroscopy (XPS) are needed. In fact, these methods allow for insight into the composition, structure, and surface chemistry of battery materials. For this reason, in the following section, the basic principles of battery operation, together with some of the aforementioned techniques, will be discussed.

Basic principles of battery operation

When a current is applied, batteries convert the chemical energy contained in their active materials into electric energy through an electrochemical redox reaction during the discharge process. In the case of a rechargeable system, the battery is recharged by reversing the process. This charge/discharge processes involve the transfer of electrons from one material to another through an electric circuit. A battery consists of one or more cells (basic electrochemical units) connected in series, parallel, or both. The cell consists of three major components: [30]

- **Negative electrode** (anode during discharge) which gives up elec-

trons to the external circuit and is oxidized during the electrochemical reaction.

- **Positive electrode** (cathode during discharge) which accepts electrons from the external circuit and is reduced during the electrochemical reaction.

- **Electrolyte** (ionic conductor) which separates the anode and cathode so they do not react directly and forces the electrons to go through the external circuit [31].

When the cell discharges, electrons and ions are at the negative electrode. The electrons pass through an external circuit and diffuse to the positive electrode, while the ions migrate through the cell to the cathode, where they undergo a chemical reaction. Figure 4 shows a schematic representation of a cell during discharge.

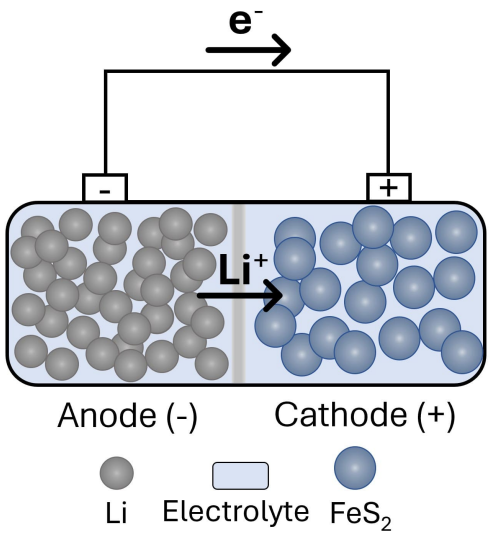

Figure 4: Lithium-metal battery with a solid cathode of iron disulfide during first discharge [31].

Two of the most important parameters for batteries are the theoretical capacity of the electrodes and the active mass ratio between the negative and positive electrode (N/P ratio). In fact, balancing active materials is essential for providing safety and cycle life [32]. To calculate the N:P ratio,

the discharge capacity (Q_{dis}, in mAh) must be assumed to be the same for both negative and positive electrodes, as shown in the equation 5 [32].

$$Q_{dis} = q_{negative} \cdot m_{negative} = q_{positive} \cdot m_{positive} \tag{5}$$

In which Q_{dis} (mAh) is the product of reversible specific capacity q (mAh g^{-1}) and the used active mass m (g) [32]. Eq. 5 can be then written as the ratio of reversible specific capacity of the positive and negative electrodes:

$$\frac{m_{negative}}{m_{positive}} = \frac{q_{positive}}{q_{negative}} \tag{6}$$

Which is, effectively, the N:P ratio. To avoid deterioration and enhance battery life, an excess capacity of negative electrodes is necessary; therefore, a N: P ratio larger than 1: 1 is required. Since the capacity of a battery is constrained by the capacity of the positive electrode [33], the theoretical battery capacity can be calculated using eq. 7.

$$\text{Battery capacity (mA)} = \text{Specific capacity of CAM (mAh g}^{-1}\text{)} \cdot \text{Mass of CAM (g)} \tag{7}$$

Moreover, to calculate the theoretical capacity of the cathode active material Equation 8 can be used [30].

$$Q_{th} = \frac{nF}{M} \cdot \frac{1}{3.6} \tag{8}$$

In which n is the number of exchanged electrons, F is the Faraday constant and M is the molecular weight of the cathode active material. The term 1/3.6 is needed to obtain the theoretical capacity in mAh g^{-1}.

2.1 Electrochemical methods

Cyclic voltammetry

Due to its ability to obtain information on complicated electrode reactions, cyclic voltammetry (CV) is a very popular technique for initial studies on new electrochemical systems [34]. In particular, CV is widely used in battery research. To start a CV measurement, the terminal voltage (E_1, E_2) and the scan rate (v) have to be chosen, then a triangle voltage is applied to the electrochemical system (Figure 5a)). In a CV test, a scan rate is applied to the electrodes and a current response is recorded. The detected current-response curve is directly related to the redox reactions that occur at the electrode / electrolyte interface [29, 35]. A typical current response for battery systems is shown in figure 5.

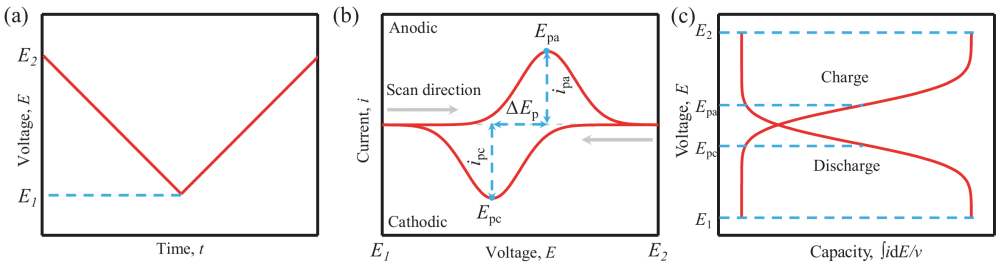

Figure 5: "a) Voltage profile applied in a CV measurement, b) current response versus voltage curves and c) voltage versus integral current curves" [29].

Useful information on the electrochemical system under investigation can be gained from the peak voltage (E_p) and peak current (i_p). Specifically, the ratio of peak current ($i_{p,a}/i_{p,c}$, where the a and c subscripts identify anodic and cathodic currents) and the difference of peak voltage (ΔE_p = Ep, a - $E_{p,c}$ can be used to judge the reversibility of an electrochemical process [35]. In cyclic voltammetries, voltage is related to electrode reactions, while current is relevant to faradic capacity. In the battery field, when CV curves are transformed into voltage versus capacity profiles (Fig. 5c)) the charge and discharge plateaus correspond to anodic and cathodic peak voltages. In battery research cyclic voltammetry is often employed to study

the electrochemical stability window of electrolytes and electrodes. This method has proven to be highly effective in extimating the voltage stability of liquid electrolytes; however, when it comes to SEs, CV can often lead to an overestimation. Additionally, sometimes the electrodes used as reference might react with the solid electrolytes leading to unreliable result. For this reason, for the study of the stability of solid-state-battery components a three-electrode setup is more suitable [36].

Galvanostatic charge-discharge

GCD measurements record the voltage response under a constant applied current. Experimentally, a controlled current is applied between the working and the auxiliary electrodes and the potential is recorded between the working and the reference electrode. The voltage response indicates changes in the electrode processes that occur at the electrode interface [34, 30]. Typically, to start a GCD measurement, one needs to choose the current that has to be applied but also the cut-off voltages at which the current direction will be inverted. The typical voltage profile that can be gained from GCD is an oblique line with one or more plateaus. These plateaus correspond to cathodic/anodic peaks in cyclic voltammetry and are related to the thermodynamics of electrode reactions [29]. GCD can be used to identify practical capacity, analyze cycling stability and rate capability, examine self-discharge characteristics, and kinetics of electrode reactions. In addition, by repeatedly charging and discharging the battery, cycle life can be calculated (number of cycles when the reversible capacity fades to 80 % of its initial value), which is one of the most important parameters for rechargeable batteries [29]. Both current (C-rate) and voltage can be modified to suit the experimental needs, however, these parameters have a fundamental role in battery degradation. As a matter of fact, deeper discharges and rapid charge/discharge rates normally accelerate the degradation processes that occur and lead to capacity loss [37].

The C-rate is the rate at which the battery is charged or discharged relative to its maximum capacity; in other words, it is the speed at which desodiation and sodiation occur in a sodium battery. Therefore, it regulates the kinetics of chemical reactions inside the electrodes. For example, charging (or discharging) at 1 C means that the cell takes 1 h to be fully charged. High C-rates indicate fast charging and discharging processes that could damage the battery's long-term health. Likewise, deep discharge can cause pronounced chemical and physical changes that lead to increased stress and faster degradation of the battery [37]. Thus, finding a suitable voltage range

and current (C-rate) during GCD experiments is of critical importance.

To calculate the C-rate of a battery, one needs to take into account the theoretical capacity of the battery and the current at which the cell is charged / discharged (equation 9) [33].

$$\text{C}-\text{rate}\ (\text{h}^{-1}) \ = \ \frac{\text{Current (mA)}}{\text{Battery Capacity (mAh)}} \tag{9}$$

Electrochemical impedance spectroscopy

The electrode processes can be studied by measuring the change in the electrical impedance of an electrode using electrochemical impedance spectroscopy (EIS). During an EIS experiment, an oscillating voltage is applied to the system (cell) and the oscillating current response is recorded [34, 30]. There are many advantages to EIS, for example, the ability to make high precision measurements, to treat the response theoretically using linearized current-potential characteristics, and the possibility of measuring over a wide time or frequency range [34].

Impedance can be seen as an extension of the concept of resistance to an alternating current; therefore, impedance (Z) can be represented as follows.

$$E = I\mathbf{Z} \tag{10}$$

In eq. 10 both the voltage (E) and the current(I) are oscillating, so they can be written as functions of the angular frequency ω, respectively as:

$$E(t) = |E|sin(\omega t) \tag{11}$$

$$I(t) = |I|sin(\omega t + \theta) \tag{12}$$

In eq. 11 $|E$ |is the amplitude of the voltage signal, ω the angular frequency ($\omega = 2\pi f$ where f is the frequency) and t the time. The current response $|I$ |is shown in eq. 12, in which θ is a phase shift due to the reactance (capacitance or inductance) [38]. Substituting eqs. 11 and 12 in eq. 10, the impedance can be expressed as follows:

$$\mathbf{Z} = \frac{E(t)}{I(t)} = |Z|\frac{sin(\omega t)}{sin(\omega t + \theta)} \tag{13}$$

Using Euler's formula for complex numbers ($e^{jx} = cos(x) + jsin(x)$, where j is the imaginary unit) the impedance can be written as:

$$E = I\mathbf{Z} = I|Z|e^{j\theta} \tag{14}$$

Typically, the impedance spectra are represented on a complex cartesian plane, so the complex impedance can be represented by separating the complex and the real part (eq. 15).

$$\mathbf{Z} = Z' + jZ'' \tag{15}$$

Z' and *Z"* are the resistive and reactive parts of the impedance, respectively [38].

Electrochemical impedance spectroscopy offers kinetic and mechanistic data of various electrochemical systems; in fact, EIS measurements at an electrochemical system can be simulated to an equivalent electrical circuit, which consists of components such as resistances, capacitors, inductors, as well as other more complicated elements connected in different ways. However, assigning each chemical and physical phenomenon to one circuit element is not trivial. The performance of a cell can be represented by an equivalent circuit of resistors and capacitors in which the current passes with the same amplitude and phase angle of the real cell under excitation. However, equivalent circuits drawn for electrochemical cells are not unique, and it is not always possible to identify circuit elements with processes that occur in cells [34].

Partial ionic and Electronic conductivities measurement

Ionic and electronic conductivities are some of the most crucial features of battery materials. They indicate how easily ions and electrons pass through the analyzed material and electrode composites [39]. To evaluate the ionic and electronic conductivities of the cathode composites, electron and ion blocking setups are used, respectively, as shown in Figure 6 .

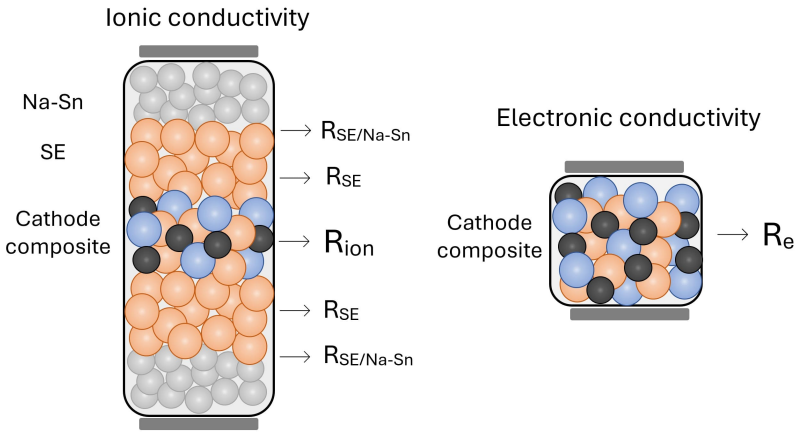

Figure 6: a) schematic of the electron blocking measurements setup for the ionic partial conductivity. b) ion-blocking measurement setup for the electronic partial conductivity. Adapted from [40].

The partial ionic and electronic conductivites can be determined using equation 16 [41].

$$\sigma = \frac{1}{R}\frac{l}{A} \tag{16}$$

In which R is the sample's resistance and, l and A are the length and the cross-sectional area of the sample, respectively. In order to evaluate the ionic and electronic conductivities, both DC and AC methods can be used. In the DC method, the current response of the voltage set-up is measured at different voltage values. Subsequently, the voltage is plotted against the current in a graph. From the slope of the obtained graph information on the resistance of the samples can be obtained, and therefore ionic and electronic conductivities can be calculated. However, to obtain the effective ionic resistance of the analyzed material (labeled R_{ion} in Figure 6) different

contributions have to be subtracted from the measured total ionic resistance $R_{ion,DC}$ as shown in the following equation:

$$R_{ion} = R_{ion,DC} - 2R_{SE} - 2R_{SE/Na-Sn} \tag{17}$$

R_{SE} is the contribution from electron blocking layers while $R_{SE/Na-Sn}$ is the contribution from the interface between the SE layer and Na-Sn. The measured electronic resistance is the actual electronic resistance of the analyzed materials, as shown in eq 18 [40]. These resistances are then used to calculate partial ionic and electronic conductivities, as shown in eq. 16.

$$R_{e,DC} = R_e \tag{18}$$

2.2 Analytics

X-ray diffraction techniques

Most methods for the determination of the atomic structure of crystallographic formations are based on the idea of scattering of radiation. X-rays are one type of radiation which can be used to achieve this. Typical interatomic distances in a solid are on the order of an Ångstrom (10^{-8} cm). Therefore, an electromagnetic probe of the microscopic structure of a solid must have a wavelength this short, which corresponds to characteristic energies for X-ray radiation. X-ray wavelengths are typically in the range of 0.1-10 Å, corresponding to photon energies of hundreds of thousands of electron volts (eV to keV range). The distribution of X-rays scattered by a periodic array of ions reveals the locations of the ions within that structure [42].

Crystalline substances give remarkably characteristic patterns of X-ray radiation diffraction. In crystalline materials, for certain sharply defined wavelengths and incident directions, intense reflections of scattered radiation (Bragg peaks) are observed. These can be accounted for by regarding a crystal as made of parallel planes of ions, spaced at a distance d. Sharp reflections appear when the reflected rays from successive planes interfere constructively. The path difference between the two rays is $2d\sin\theta$, where θ is the angle of incidence, which varies during the experiment, as shown in Figure 7. For rays to interfere constructively, this path difference must be a whole multiple of wavelengths, as stated in Bragg's law:

$$n\lambda = 2dsin\theta \tag{19}$$

The integer n is known as the order of the corresponding reflection. For a beam of X-rays containing a range of different wavelengths, many different reflections are observed [42].

The diffraction patterns contain contributions from several micro- and macrostructural features of a sample. For instance, from the position of

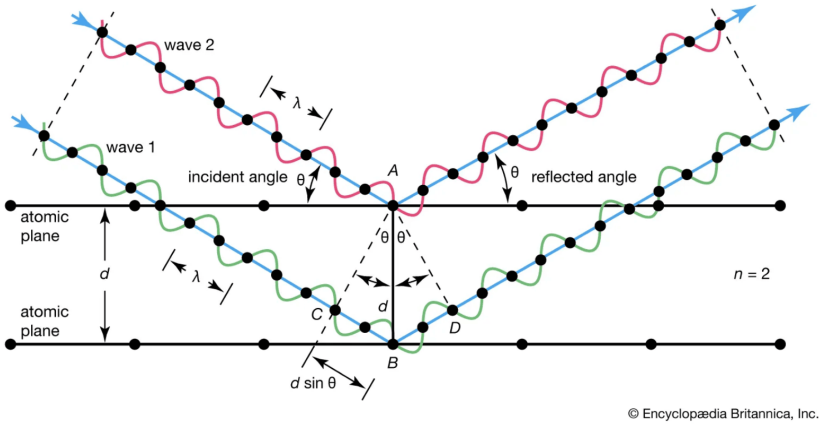

Figure 7: The diagram shows waves 1 and 2, in phase with each other, glancing off atoms A and B of a crystal that has separation distance d between its lattice planes [43].

the reflections one can investigate lattice parameters, space group, chemical composition, macrostresses, and qualitative phase analysis. Based on the diffraction peak intensity, information about crystal structure (atomic positions, temperature factor, or occupancy) as well as texture and quantitative phase analyses can be obtained. Finally, the reflection shape gives information on broadening contributions such as microstrains and the crystallite size of the sample. XRD methods are widely used for the identification of present phases (qualitative analysis) and for the determination of their respective amounts (quantitative analysis). This can be done because different lattice planes are in diffracting conditions, which implies that intensity variations can come from a preferred orientation. In fact, each phase produces a characteristic diffraction pattern that allows its identification. Moreover, when several phases are present in a system, the characteristic patterns of all phases are respectively proportional to their amounts [44].

Scanning Electron Microscopy and Energy-Dispersive X-Ray Spectroscopy

Scanning electron microscopy (SEM) allows the observation and characterization of materials on a nanometer (nm) to micrometer (μm) scale. In SEM, the analyzed area is irradiated with a finely focused electron beam, and from the interaction of such beam with the samples, different signals are produced. These signals include secondary electrons, backscattered electrons, characteristic X-rays, and other photons of various energies from which information on the analyzed samples can be gained. For example, the signals coming from secondary and backscattered electrons give information on the surface topography of the samples, while the analysis of the characeristic x-radiation emitted from the samples yields qualitative identification and quantitative elemental information [45]. To study elemental composition and distribution, energy-dispersive X-ray spectroscopy (EDS) is commonly used. The EDS detector can be integrated in both SEM and transmission electron microscopy (TEM) systems and the measurements are carried out at high energy. SEM-EDS typically provides compositional information from the near-surface region. The surface of the analyzed material is excited by an energy source (typically high-energy electrons that have sufficient energy to excite characteristic X-rays of the elements present) that knocks off a core-shell electron, thus leaving a vacancy. An electron in the material at higher energy level then proceeds to fill its place, releasing the difference in energy as an X-ray that has a characteristic spectrum based on its atom of origin (with the exception of lighter elements such as Li, Be and B). This energy is then detected by an EDS detector where the emitted X-rays are represented in a form of a spectrum, mapping or line. The position of the peaks in the spectrum identifies the element, while the intensity of the signal corresponds to the concentration of the element. Adding an EDS detector to an electron microscope can provide compositional information on the sample analyzed down to the micrometer to submicrometer scale [46, 47].

X-ray Photoelectron Spectroscopy

X-ray photoelectron spectroscopy is one of the most widely used techniques in different fields because it provides information on the chemical composition of a sample. In fact, this technique is employed in the areas of material science, chemistry and chemical engineering because it allows a detailed study of surface and interface properties [48]. In battery research XPS is adopted to investigate interfacial properties of battery components which are essential for the understanding of surface chemistry, composition, and impurity presence [49].

XPS is particularly appealing because of its surface sensitivity. In fact, the samples under analysis are irradiated with monoenergetic soft X-Rays (energies lower than ≈6 keV) and the kinetic energies of the electrons emitted by the photoelectric effect are recorded. From the kinetic energies of the photoelectrons, information on the chemical state of the materials inside the samples can be gained [50, 51]. This is possible because the kinetic energies of the emitted electrons is correlated to the binding energy of the atomic orbital from which the electron originates (BE), as shown in eq 20.

$$KE = h\nu - BE - \phi_s \tag{20}$$

In which KE is the kinetic energy of the photoelectron, $h\nu$ is the energy of the photon and ϕ_s is the spectrometer work function. The binding energy is the energy difference between the initial and final state after the electron has left the atom [50]. The XPS spectrum is plotted as the number of detected electrons per energy interval against their kinetic energy. Each element has a unique spectrum and all elements except hydrogen and helium can be detected [50, 51]. Because of this, XPS is a powerful technique to identify and determine the concentration of different elements in the surface. Sometimes shift in the elemental binding energies (chemical shifts) can be detected, these come from chemical potential and polarizability difference of the various compounds. The chemical shifts are used to determine the chemical state and the chemical environment of the atoms present in a

sample [50, 51].

In addition to the electrons emitted during the photoelectric process, Auger and fluorescent X-ray photon can be emitted. Figure 8 shows a comparison between these three processes.

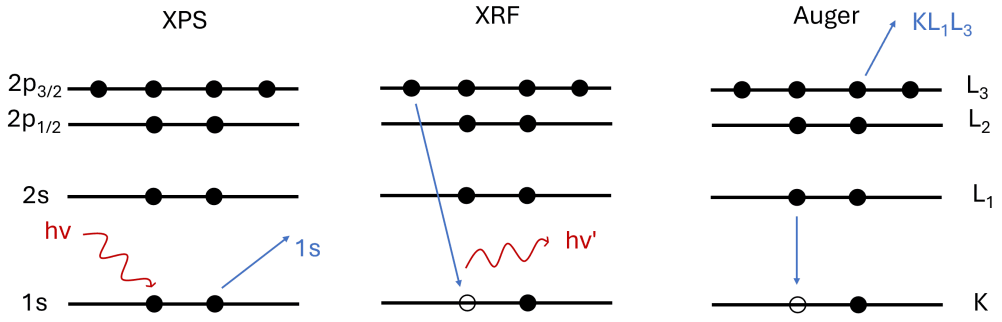

Figure 8: "Processes that result from x-ray bombardment of a surface include (a) emission of a photoelectron, (b) x-ray fluorescence, and (c) emission of an Auger electron". Adapted from [51].

Usually, in this energy range the fluorescence emission is a minor process. On the other hand, Auger electrons are detected by the instrument. In the Auger process, an outer electron falls into the vacancy of the inner orbital formed after the photoemission. Simultaneusly, a second electron is emitted, thus releasing the excess energy. The kinetic energy of Auger electrons is independent of the mode of the initial ionization. Therefore, the photoionization process usually leads to the emission of two electrons: a photoelectron and an Auger electron [50].

XPS is a surface-sensitive technique because, even though X-rays can penetrate a few μm into the sample, not all the electrons are able to escape the material surface. In fact, the electrons that are generated too deep in the material will encounter inelastic collisions, leading to energy loss and inability to escape the sample [51]. Only the electrons that are generated within tens of angstroms below the solid surface can leave the material and are responsible for the peaks in the XP spectra [50].

3 Experimental

3.1 Materials and sample preparation

Preparation of FeS_2. Commercially available iron disulfide, powder, -325 mesh, 99.8% trace metals basis (Merck-Sigma-Aldrich GmbH) was used as starting material. The commercial powder was ball milled under Ar atmosphere ($p(O_2)/p < 5$ ppm, $p(H_2O)/p < 5$ ppm) with a Fritsch Pulverisette 7 premium line mill (ZrO_2 milling set, 80 mL cups, 5 mm diameter milling media) to reduce its size. Milling was conducted for 12 milling cycles, each of 10 min at 500 rpm followed by 10 min break.

Preparation of all-solid-state positive electrode composites. Positive electrode composites for all-solid state Na-S cells were prepared by using the milled FeS_2 powder, Na_3PS_4, and commercially available Super P conductive carbon black (CB) (MSE supplies). Other positive electrode composites were prepared by substituting Na_3PS_4 with $Na_{2.8}P_{0.8}W_{0.2}S_4$. The solid electrolytes used were synthesized in the laboratory. Before mixing the components, FeS_2 and carbon black powders were dried for 24 h at 300 °C under a dynamic vacuum in a Büchi oven. The positive electrode composites were prepared by ball mill. To prepare the composites, a Fritsch Pulverisette 7 premium line mill (ZrO_2 milling set, 80 mL cups, 5 mm diameter milling media) was employed. The ball milling was conducted for 3 milling cycles of 10 min at 300 rpm each followed by a 10 min break, and with a media-to-sample weight ratio of 10:1 and 20:1. Positive electrode composites containing FeS_2 were prepared by mixing CAM:SE:CB in 40:50:10 weight ratio (CAM 40 wt.%, SE 50 wt.% and CB 10 wt.%). The carbon and the SE were used within the composite to ensure sufficient electronic and ionic contact of FeS_2. Due to the instability of the materials to ambient atmosphere, all samples were always handled under Ar atmosphere ($p(O_2)/p$ <5 ppm, $p(H_2O)/p$ <5 ppm).

Preparation of the negative Na-Sn alloy electrode. Na-Sn was

prepared in argon atmosphere ($p(O_2)/p$ <5 ppm, $p(H_2O)/p$ <5 ppm) in batches of 2.0 g by ball milling. Tin powder (100 mesh, 99.999 % from Fisher Scientific GmbH) was alloyed with elemental Na (BASF SE) in different ratios for the two alloys. Na-Sn A was prepared with 43 % wt. of Na and 57 % wt. of Sn, Na-Sn B was prepared using 40 % wt. Na and 60 % wt. Sn. The media-to-sample weight ratio was varied for the two different alloys. Respectively, 5 and 10 mm ZrO_2 balls were used in a 45 mL ball milling cup. The synthesis was carried out with different ball milling procedures for the two alloys. Table 1 shows all the parameters used to synthesize different types of Na-Sn alloy.

Table 1: Different Na-Sn alloys and their synthesis procedures.

Alloy	**Milling-break** (min)	**Media / sample weight ratio**	**Speed** (rpm)	**Number of cycles**	**Na / Sn weight ratio** (%)
Na-Sn A	15-5	30 : 1	600	30	40 / 60
Na-Sn B	10-10	35 : 1	550	60	43 / 57

Sample preparation for ex situ analyses. After cycling at a low C-rate (0.02 C), the potential was held for 24 hours. The samples were then stabilized at their OCV. The cells were then carefully removed from the cell casing in an Ar-filled glovebox with a hand press. The cross sections were prepared with a Leica EM TIC 3X (Leica Mikrosysteme GmbH). These were cut under vacuum (10^{-6} mbar) for 4 hours using three ion guns (6.0 kV and 2.2 mA) and in cryo conditions, liquid nitrogen was used to cool them at -100 °C. The samples were always transferred with a Leica VCT500 air-tight transfer module. Directly after cutting, SEM and EDS analyses were performed on the cross sections.

3.2 Cell assembly

Cell assembly for long-term cycling. All-solid-state Na-S cells were assembled in custom-made PEEK casings with 10 mm inner diameter. 60 mg of Na-Sn alloy were employed as negative electrode and 5 mg of cathode composite as positive electrode. 70 mg of SE were used. For densification, the layers (anode, SE and cathode) were compressed uniaxially for 3 min at 3 tons. Two polished stainless-steel rods were employed as current collectors. The cells were fixed in a frame and a pressure of approximately 60 MPa was applied to guarantee mechanical contact during cycling.

Cell assembly for partial conductivity measurements. All cells for electronic partial conductivities were assembled in custom-made PEEK casings with 6 mm inner diameter. For measurements, ca. 100 mg of positive electrode composite was loaded. All cells for ionic partial conductivities were assembled in custom-made PEEK casings with a 10 mm inner diameter. For measurements, ca. 50 mg of positive electrode composite was loaded between to layers of solid electrolyte (70 mg each). On both sides Na-Sn alloy was used. For all measurements, two polished stainless-steel rods were employed as current collectors. For densification, the layers were compressed uniaxially for 3 min at 1.1 tons (for 6 mm diameter cells) or 3 tons (for 10 mm diameter cells). The cells were fixed in a frame and a pressure of approximately 60 MPa was applied to guarantee mechanical contact during electrochemical testing.

3.3 Characterization

Electrochemical impedance spectroscopy measurements. For all measurements, a potentiostat (BioLogic VMP 300, Seyssinet-Pariset, France) was used. All measurements were conducted at 25 °C. The pressure loading of all cells was 60 MPa. An amplitude of 10 mV was chosen, and the frequency range was 7 MHz to 10 mHz. The Na-ASSB cell impedance was measured directly after cell assembly and after charge and discharge.

Electrochemical testing. Battery cycling was performed at 25 °C with a VMP300 or a VMP-3 potentiostat (Biologic). All cells for long-term cycling were tested under galvanostatic conditions in the potential range of 0.5 - 3.0 V *vs.* Na-Sn, with 15 minutes of OCV between each step. A four-electron reaction of FeS_2 was assumed for calculating the C-rates, so the theoretical capacity of FeS_2 (894 $mAh \cdot g^{-1}$) was used. For the characterized model cells, rate of 0.1 (179 $\mu A \cdot cm^{-2}$) were used. All cells used for the evaluation of long-term cycling performances were built as duplicates to ensure reproducibility. Partial electronic conductivity measurements were performed by impedance and chronoamperometry. The latter method was employed also for partial ionic conductivity. The impedance was measured with an amplitude of 10 mV and in a frequency range of 7 MHz−100 mHz. The impedance spectra were fitted by using the RelaxIS 3 software package (rhd Instruments, Darmstadt, Germany).

Cyclic voltammetry. For CV testing, press cells as previously described were used. After assembly each cell was allowed to equilibrate for 24 h to establish a stable OCV prior to any measurements. The stepwise CV experiments were performed using a VMP300 potentiostat (Biologic) at a constant temperature and scan rate of 298 K and 0.05 and 0.1 mV/s, respectively. Each experiment started at the open-circuit voltage (OCV), the potential was swept until 3.2 V and then back to 0.5 V *vs.* Na-Sn, and the cycle was finalized at the OCV. Three consecutive cycles were measured for each sweep.

Particle Size Analysis (PSA). PSA measurements were performed with a HELOS/BR (Sympatec GmbH) instrument with laser diffraction at 25 °C. The measurements were performed in dispersion. The dispersing media for the solid electrolytes was a mixture of xylene-Oppanol (1 wt %). A quartz cuvette with a volume of 6 mL was employed. The data was exported using the PAQXOS software.

X-ray diffraction (XRD). XRD analysis was performed in Bragg-Brentano geometry on a reflection transmission spinner. The samples were analyzed with an Empyrean 3 diffractometer (Malvern PANalytical) with Mo-Kα source (60 kV, 40 mA). The 2θ range was 5°–45° and with a step size of 0.014°.

Scanning electron microscopy (SEM). SEM analysis was performed using a Carl Zeiss Merlin electron microscope with an acceleration voltage of 3 kV, aperture size of 20.0 μm, and in vacuum (10^{-6} mbar). The software used was SmartSEM.

Energy dispersive X-ray spectroscopy (EDS). EDS analysis was performed within the SEM using an X Max 50 Silicon Drift Detector (Oxford Instruments) with a polymer window. An acceleration voltage of 10 kV and an aperture size of 60.0 μm were used at a working distance of 8.5 mm. The software used for the elemental analyses was AZtec 6. The cross sections of the post mortem samples were analyzed first with SEM and then with EDS.

X-ray photoelectron spectroscopy (XPS). XPS measurements were conducted by using a PHI VersaProbe IV system (Physical Electronics Inc.). A monochromated Al K X-ray source (Xray source 50 W 15 kV with beam diameter of 200 m) was used. A step time of 20 ms, a step size of 0.2 eV, and an analyzer pass energy of 55.00 eV were used for the detailed spectra. During measurements, the sample surface was charge-neutralized and the pressure ranged from 10^{-7} to 10^{-6} Pa. The samples were prepared in a glovebox (M. Braun Inertgas-Systeme GmbH, (O2 $<$ 5 ppm, H2O $<$ 5 ppm) and transferred from the glovebox to the analysis chamber with

a transfer shuttle. The samples were mounted on a sample holder using insulating tape and with the exposed positive electrode surface facing the X-ray beam. The samples were sputtered with a gas cluster ion beam gun (GCIB) (10 Kv 30 nA, 2 × 2 mm2, 5 min) and Argon clusters to clean the surfaces. Data analysis was performed by using CasaXPS software. The detailed fitting of the XP spectra are shown in Tables 2.

Table 2: Carbon 1s (RSF 0.314) components' constraints used for calibration.

Component	**Line shape**	**Binding energy constraint** (eV)	**FWHM**
C-C C-H	GL(30)	284.8	1.0-1.5
C-O	GL(30)	C-C C-H + 1.3 eV	1.0-1.5
C=O	GL(30)	C-C C-H + 2.8 eV	1.0-1.5
O-C=O	GL(30)	C-C C-H + 4.0 eV	1.0-1.5

Table 3: Sulfur 2p (RSF 0.820) components' constraints.

Component	**Line shape**	**Binding energy constraint (eV)**	**FWHM constraint**	**$2p^{1/2}$ to $2p^{3/2}$ (eV)**
PS_4^{3-}	GL(30)	161–160.6	1.0–1.7	+1.2
P=S	GL(30)	161.7–160	1–1.7	+1.2
S_2^{2-}	GL(30)	163.5–162	0.7–1.5	+1.18
S_x	GL(30)	164.8–164.1	0.7–1.5	+1.18
SO_x	GL(30)	169.8–169.2	0.7–1.5	+1.18

Table 4: Phosphor 2p (RSF 0.605) components' constraints.

Component	**Line shape**	**Binding energy constraint (eV)**	**FWHM constraint**	$2p^{1/2}$ **to** $2p^{3/2}$ **(eV)**
PS_4^{3-}	GL(30)	131.7–128.5	0.5–1.7	+0.89
PO_4^{3-} / P=S	GL(30)	134–132.7	0.5–1.7	+0.89
PO_3^{-}	GL(30)	135–133.7	0.5–1.7	+0.89

4 Sodium-Tin alloy as negative electrode

Although all solid-state batteries promise enhanced energy densities compared to lithium-ion batteries (LIBs), this can only be achieved if metal anodes or anode free setups are employed [11]. However, in practical sodium solid-state batteries that use sulfide-based SEs, this cannot be done due to the poor interfacial stability between the SE (low reduction stability of the SEs) and the metal electrode [52]. In particular, it has been shown that Na_3PS_4 is highly unstable when in contact with Na metal electrodes, leading to the formation of several decomposition products (i.e. Na_2S, Na_3P and sodium polyphosphides) [52]. The formation of these interfacial side products deteriorates the interface between Na and the SE, thus bringing an increase in interphase resistance that leads to a decay of the cell performance [52]. In solid-state batteries understanding the stability of the anode in contact with solid electrolyte is essential. If the solid electrolyte is thermodynamically stable against Na metal, then the interface between the two materials will be stable. On the contrary, if the SE is not stable against the metal anode, it might decompose forming different types of interlayers [23, 52].

There are three main types of interphase layers:

- Ionically insulating and electronically conducting layer
- ionically conducting and electronically conducting layer
- ionically conductive and electronically insulating layer

Figure 9 shows a schematic representation of the different types of interphase.

The electronically conducting interlayers will continuously grow after every cycle, leading to irreversible consumption of Na^+ inventory. Usually, the observed interphase layers are ionically and electronically conducting, also known as mixed-conducting interface (MCI). MCI constantly grows, leading to a significant capacity fade during cycling [23]. Because of the

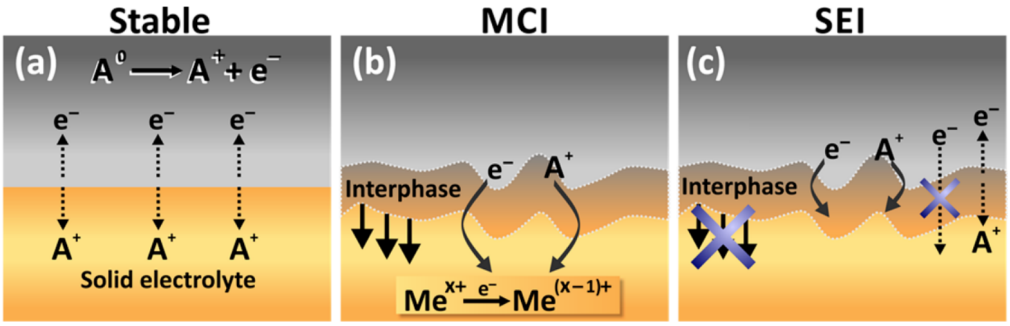

Figure 9: "Three different possible types of interphases: (a) a stable interface, (b) the mixed-conducting interphase, and (c) the solid electrolyte interphase, which only conducts ions. While the formation of a mixed conducting interphase always deteriorates the battery performance, the formation of an SEI may be favorable if a good ionic conductor forms". Adapted from [52]

high instability of Na_3PS_4 in contact with Na metal (constantly growing interphase), a suitable substitute to replace either one of them has to be found. In this context, alloy anodes seem promising; in particular, for Na-based batteries, the alloy elements in Group IVA stand out as anode materials [53]. Among the alloys formed between Na and the elements from Group IVA, sodium-tin alloys are gaining increasing attention. The Na-Sn phase diagram shows eight thermodynamically stable alloys: $NaSn_6$, $NaSn_4$, $NaSn_3$, $NaSn_2$,NaSn, Na_9Sn_4, Na_3Sn, and $Na_{15}Sn_4$. Figure 10 shows the Na-Sn phase diagram together with the voltages at which the sodiation of tin occurs [54]. The sodiation / desodiation curves at ambient temperature show four distinct plateaus, highlighting the fact that different Na-Sn phases are formed. Figure 10 diagram clearly shows that the last three plateus correspond to the formation of NaSn, Na_9Sn_4, and $Na_{15}Sn_4$. However, many of the two-phase regions indicated in the equilibrium phase diagram are absent in the voltage curve [54].

The setup investigated in this work is composed of a composite cathode (FeS_2 / Na_3PS_4 / carbon black), Na_3PS_4 as separator and a Na-Sn alloy anode. The alloy chosen for this investigation is Na_15Sn_4 due to its high capacity (847 mAh g^{-1}) [53]. During cycling, the charge curves (desodiation of the positive electrode) show the formation of voltage spikes, as shown in Figure 11a. These voltage spikes appear as soon as the third/ fifth cycle and

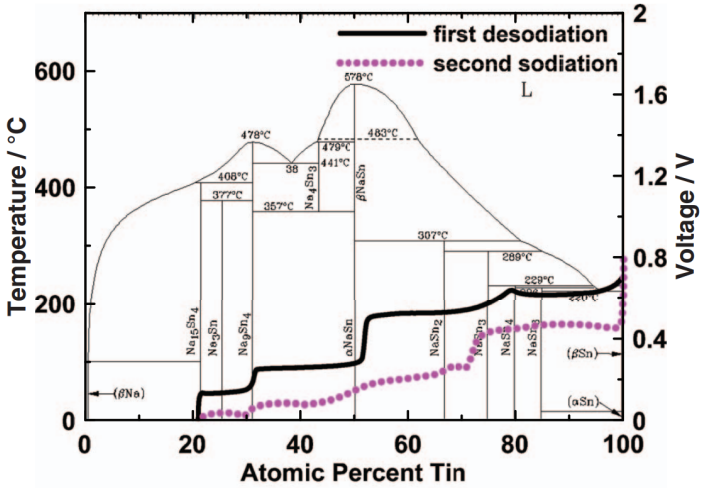

Figure 10: Voltage curves of the first desodiation and second sodiation of tin superimposed on the Na-Sn binary phase diagram [54]. The voltage is reported against Na / Na^+.

get more pronounced in every subsequent charge; leading in the worst cases to short circuits (Fig. 11b). This charging behavior reflects in unreasonable high charge capacities (the capacity grows from approximately 0.6 to 4 mAh g^{-1}) that lead to coulomb efficiencies lower than 20 %. Additionally, the voltage spikes seem to have a capacity-dependent behavior. As a matter of fact, they are not present for cells that deliver capacities lower than 0.1 mAh. Moreover, the spike behavior is completely suppressed during discharge (sodiation of the positive electrode).

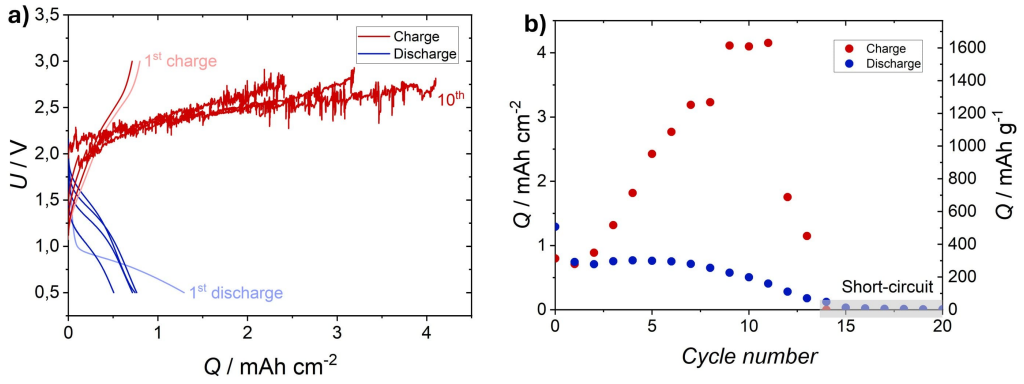

Figure 11: a) Voltage spikes appearing during charge. b) Effect of voltage spikes on the charge capacity of the cells.

A possible explanation for this is the Na-Sn alloy used in combination with Na_3PS_4 solid electrolyte, in particular the interphase forming between

the two materials might not be stable. This behavior has already been observed and can be explained with the formation of dendrites during charge that are eliminated during discharge [55].

To assess the interphase stability and understand its contribution to the charging behavior, two sodium-tin alloys were synthesized with different ball milling procedures, starting from what reported by Goodwin *et al.* [56]. Subsequently, their stability was investigated using electrochemical impedance spectroscopy.

4.1 Interphase instability

To assess the role of interphase instability on spike formation and on cell performance, two different Na-Sn alloys were tested in a half-cell setup with Na_3PS_4 solid electrolyte and a pyrite-based composite cathode (FeS_2 / Na_3PS_4 / carbon black). Specifically, two different Na-Sn alloys were synthesized via ball milling with different procedures. Table 5 summarizes the procedures employed for the synthesis.

Table 5: Synthesis parameters used for the two Na-Sn alloys.

Sample	**speed** (rpm)	**number of cycles**	**Na / Sn weight ratio** (%)
Na-Sn A	600	30	40 / 60
Na-Sn B	550	60	43 / 57

The parameters used were chosen on the basis of the work by Goodwin *et al.* [56]. In particular, in the synthesis of Na-Sn B, harder milling procedures (double the number of milling cycles) were employed to ensure the complete alloying of Na and Sn. Furthermore, for Na-Sn B, Na and Sn were mixed in a stochiometric ratio for $Na_{15}Sn_4$, while for Na-Sn A the Na / Sn weight ratio was chosen to obtain a mixture of Na_9Sn_4 and Na15Sn_4. To investigate structure and morphology of the synthesized alloys, pristine Na-Sn A and B powders were studied with XRD and SEM. In particular, these techniques were used to assess which alloy was formed after the synthesis and to compare the two. However, XRD can only detect crystalline phases. Figure 12 shows a comparison between the diffraction patterns and

the morphology of the two alloys under investigation.

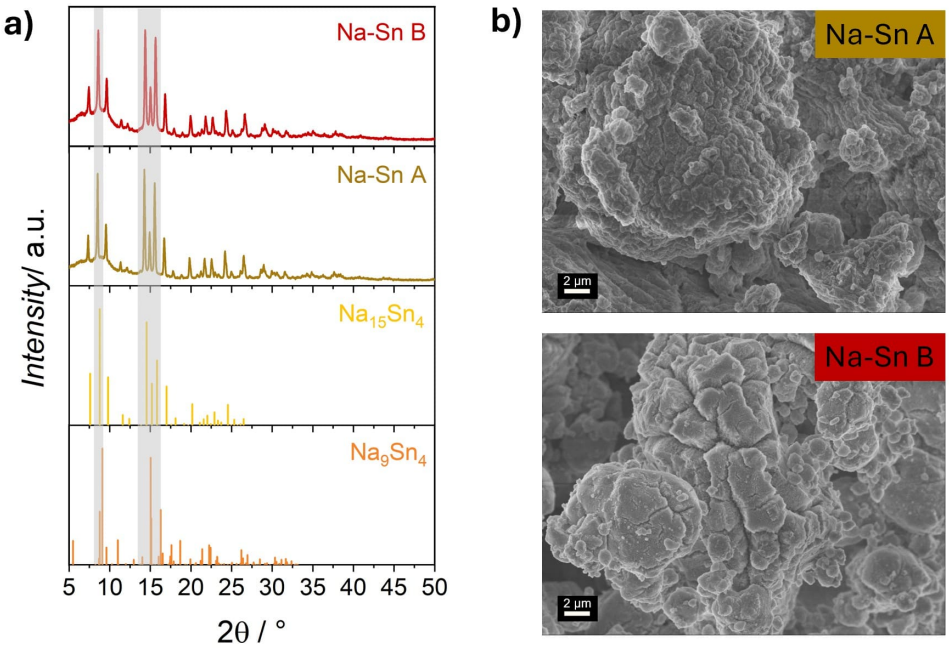

Figure 12: a) Diffraction patterns of the two synthesized alloys and those of $Na_{15}Sn_4$ and Na_9Sn_4 for comparison [57]. b) SEM images of the the alloys under investigation taken with an Inlens detector at the same magnification.

XRD patterns (Figure 12a) show the presence of the same reflections for Na-Sn A and B. Moreover, the most intense reflections present in the diffraction patterns of Na-Sn A and B coincide with the reflections of both $Na_{15}Sn_4$ and Na_9Sn_4. Not all the thermodynamically stable phases of sodium-tin are crystalline; therefore, they cannot be detected. Goodwin *et al.* reported the diffraction pattern of the Na-Sn alloy that partially matches (same reflections from 5 ° to 20 °) those measured in this work, suggesting the presence of $Na_{15}Sn_4$ and Na_3Sn [56]. Likewise, the SEM pictures (Fig. 12b) do not show great difference between the two alloys.

To effectively assess the stability of the Na-Sn / SE interphase, electrochemical impedance spectroscopy was employed. In particular, cells with the two different alloys were cycled and EIS was recorded during the OCV step. Figure 13 shows the time evolution of impedance spectra recorded every hour for 12 h during the OCV step.

From Figure 13 it can be clearly seen that Na-Sn B is more stable compared to Na-Sn A. In fact, Fig. 13 shows that for Na-Sn A, the resistance

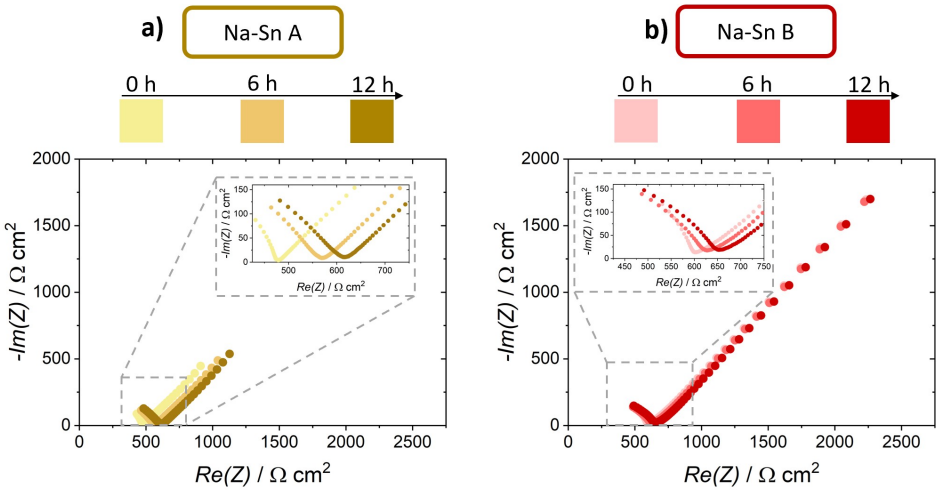

Figure 13: Time evolution of impedance spectra for a) Na-Sn A |Na_3PS_4 |FeS_2 / Na_3PS_4 / carbon black and b) for Na-Sn B |Na_3PS_4 |FeS_2 / Na_3PS_4 / carbon black cells.

increases of more than 100 Ω·cm in 12 h, while for Na-Sn B, the resistance growth is only 50 Ω·cm . This could be due to an increase of interphase resistance with time that could lead to enhanced solid electrolyte degradation and deterioration of cell performance. This might be explained with the presence of more unreacted sodium in the Na-Sn A alloy as a result of the different synthesis procedures. To further investigate this effect, cells with both Na-Sn A and B as negative electrodes were cycled. Figure 14 shows the cycling curves for these cells and the capacity retentions calculated between the 2^{nd} and the 20^{th} cycle. The discharge curves show that initially the cells with Na-Sn A (less stable interphase) deliver higher capacities than those with Na-Sn B (more stable).

However, capacity retention improves from 86 % for cells with Na-Sn A to 128 % for cells with Na-Sn B (Fig. 14b). These results show that the interphase stability plays an important role in the overall performance of a battery. In particular, higher instabilities may lead to the formation of decomposition products that, on the one hand contribute to the decline of the cell performance (worse capacity retentions) and, on the other hand may lead to additional apparent capacities [52].

Nevertheless, for both Na-Sn A and Na-Sn B cells the spike behavior

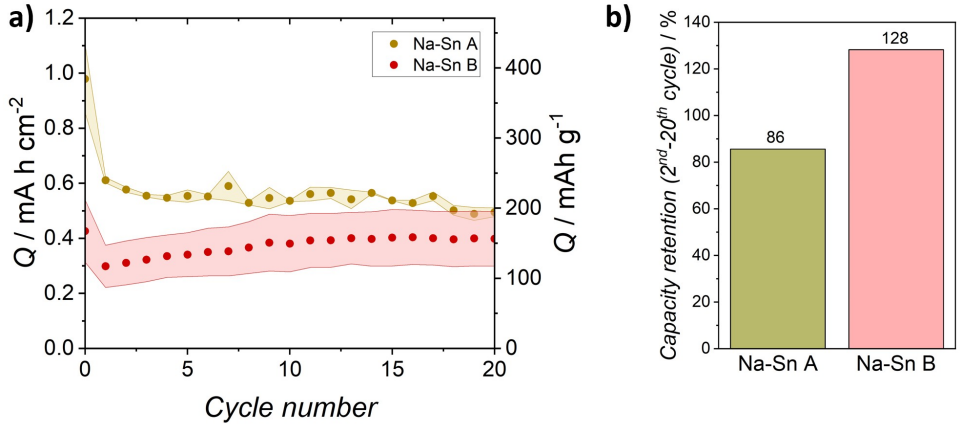

Figure 14: a) Discharge capacity *vs.* cycle number plot for half cells with both Na-Sn A and Na-Sn B and b) their capacity retentions.

persists (Figure 15). The spike behavior is less significant in the case of Na-Sn B, which means that it takes more cycles for the spikes to form and they are less pronounced. However, their appearance and the observation that in both cases they lead to extremely low Coulomb efficiencies (Figure 15 b) highlight that, in addition to interphase instability, some other mechanism might be playing a role in the formation of spikes.

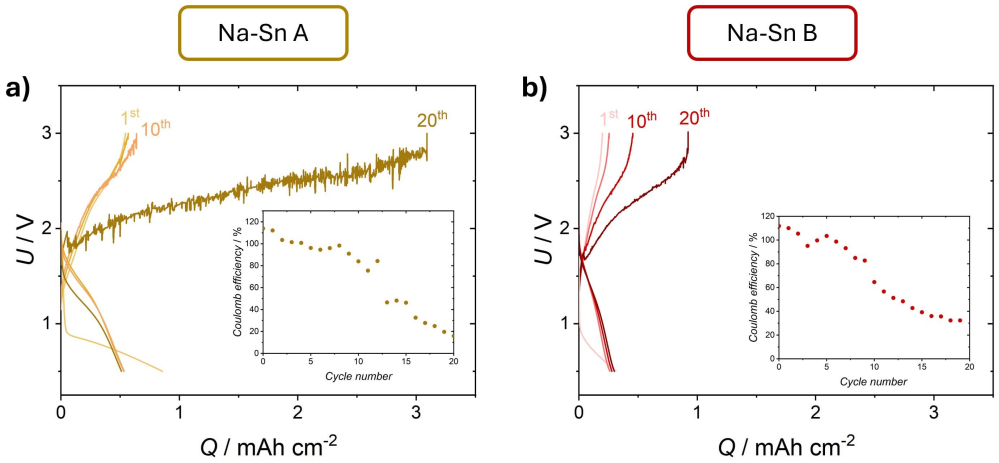

Figure 15: Voltage spikes and coulomb efficiencies for a) Na-Sn A $|Na_3PS_4|FeS_2$ / Na_3PS_4 / carbon black and b) for Na-Sn B $|Na_3PS_4|FeS_2$ / Na_3PS_4 / carbon black cells.

A possible explanation for this behavior lies in the fact that the MCI formed between the anode and the SE has a high electronic conductivity that leads to dendrite formation [55]. In fact, the formation of spikes has

been reported and studied by Yuan *et al.*; they showed the formation of hollow regions at the SE-anode interface that could promote localized dendrite growth [55]. This phenomenon can be explained with a "soft short circuit" or "dynamic short circuit" model. In this model, the short circuit path forms at the interface between the anode and the SE and penetrates into the solid electrolyte during stripping of the positive electrode (desodiation of the positive electrode, charge in this case). This happens because of the possible accumulation of electronically conductive Na-rich phases at the interphase between Na-Sn and the SE. However, when the positive electrode is plated (sodiation of the positive electrode, discharge in this case), the short-circuit path is temporarily eliminated [58]. Furthermore, since electron transport in the MCI is enhanced at high capacities and under high currents, the spike behavior is highly dependent on cell capacity [59]. To further analyze this behavior, various analytical techniques can be employed. For example, XPS and time of flight secondary ion mass spectrometry (TOF-SIMS) can be used to detect the different products forming at the interphase between Na-Sn and Na_3PS_4.

In conclusion, this study highlights the importance of a stable anode / SE interphase. In fact, interface instability has proven to have a critical effect on the cell performance. Moreover, additional studies are necessary to find ways to inhibit dendrite growth and suppress spike behavior. For experimental reasons, for the further studies performed on the positive electrode, Na-Sn A was employed.

5 Positive electrode microsctructure

In practical cells, pyrite cannot be used alone because of its semiconductor properties. In fact, large amounts of ion (SE) and electron conductive (carbon) species have to be integrated in the cathode to ensure sufficient ionic / electronic conductivity. This leads to two main issues; first, the addition of conductive species reduces the active material fraction inside the cathode, thus lowering the energy density of the cell. In addition, electrochemical reactions, which are responsible for cell capacity, occur at the triple phase boundary between FeS_2, SE, and carbon. Therefore, good contact between the different materials within the cathode is a necessary requirement for suitable battery performances [5, 13]. For this reason, cathode microstructure plays a fundamental role in pyrite-based Na-S solid-state batteries and needs to be investigated.

The influence of positive electrode microstructure for a range of different active materials and composites has been widely studied. In general, reducing the particle size within cathode composites leads to better cell performance [60, 61, 62]. In fact, a smaller particle size can help limit the formation of voids due to particle mismatch [62, 63], improve active material utilization, and could partially alleviate volume changes [60]. In addition, a good ionic conductivity is necessary inside the composites, since the main bottleneck for Li-S SSBs is the effective macroscopic ion transport in the composite. Therefore, finding solid electrolytes that possess high ionic conductivities and small particle size is the key to improving battery performance [61]. For this reason, in the following section, the influence of cathode microstructure on battery performance will be discussed. To do this, composites with FeS_2, carbon black and two different solid electrolytes (Na_3PS_4 and W-doped Na_3PS_4) were prepared with different ball milling procedures and the influence of microstructure on the electrochemical performance of cells was assessed.

5.1 Basic properties of the solid electrolytes

In this work, two different sulfide SEs were investigated as catholytes. In particular, Na_3PS_4 (NPS) and tungsten-doped Na_3PS_4 ($Na_{2.8}P_{0.8}W_{0.2}S_4$, NPWS) were examined. Tungsten-doped SEs are considered particularly suitable within cathode composites because of their high ionic conductivities. In fact, while the ionic conductivity of NPS is 0.17 mS cm^{-1}, the W-doped version can reach up to 14.7 mS cm^{-1}, making it exceptionally suitable as a catholyte [64]. However, to ensure optimal cycling performance, SEs inside the composite need to have not only good ionic conductivity but also small particle size. For this reason, an investigation of the particle size, composition, and morphology of these solid electrolytes was carried out. To do this, different characterization techniques were employed, such as SEM, particle size analysis, and XPS.

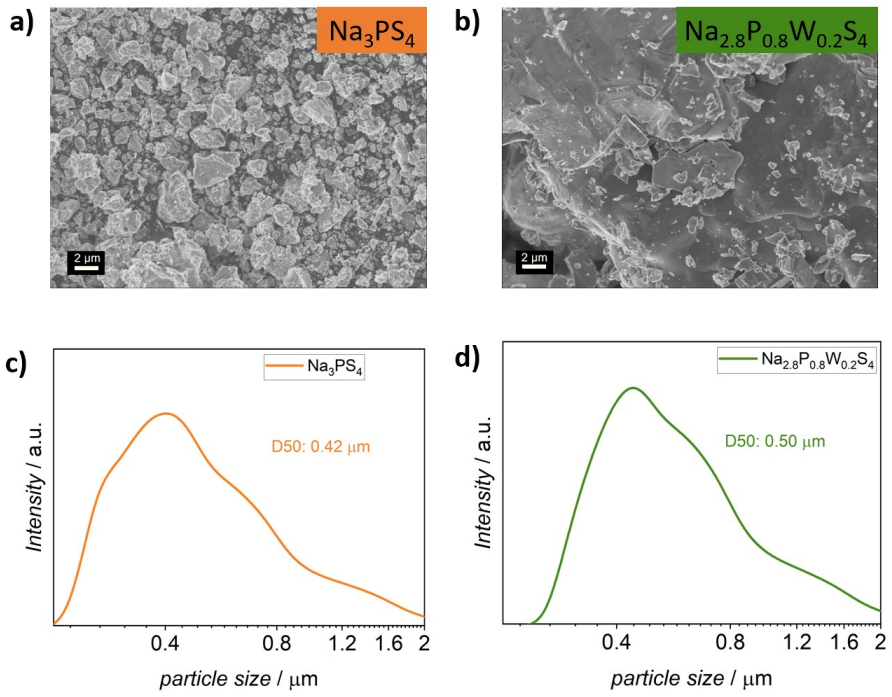

Figure 16: SEM images of a) Na_3PS_4 and b) $Na_{2.8}P_{0.8}W_{0.2}S_4$ taken with an Inlens detector at the same magnification. c) Particle size distribution for NPS and NPWS. The measurements were performed dispersing the particles in a mixture of xylene and oppanol (99:1 wt %).

Particle size and morphology were qualitatively investigated form SEM

and a laser particle size analyzer, as shown in Figure 16. Both SEM images (Fig. 16a and b) and the particle size distribution (Fig. 16 c and d) show that the tungsten-doped SE has a slightly higher particle size compared to the undoped one (D50 = 0.42 μm for NPS and 0.50 μm for NPWS), which is due to the synthesis procedures [64]. This might have an impact on the overall cell performance; therefore, strategies to effectively incorporate it in composites have to be investigated.

To study the composition and detect the presence of possible contaminants, X-ray photoelectron spectroscopy was employed. For calibration, the C1s spectra of adventitious carbon was used, see table 2 in the experimental section. Figure 17a shows the survey spectra of both NPS and NPWS. The survey spectra indicate that there is no significant contamination of the samples. In addition, the highlighted region shows the presence of tungsten in the W-doped NPS. The visible peak in the NPS spectra (Fig 17a, gray region between 25 and 40 eV) can be attributed to the presence of Na2p peak that partially overlaps with the W4f peaks.

In line with the chemical state expected for Na_3PS_4, the S2p spectra can be deconvoluted into two spin-orbit doublets, one with the main peak at 160.9 eV, and the other at 161.4 eV. A possible assignment for these doublets is that the former corresponds to $PS_4{}^{3-}$ which is expected in the structure of Na_3PS_4 [25]. The latter may be related to P=S. This assignment would be in agreement with literature [52, 64]. The doublet with the main peak at 132.2 eV in the P2p spectra of both NPS and NPWS could possibly be attributed to the solid electrolyte- P=S peak, already present in the S2p spectra, or the presence of phosphates (PO_x). The detailed O1s spectra of the SEs (fig. 17 d) further shows the possible presence of PO_x species. The presence of oxidized species in the P2p spectra could stem from the synthesis precursors [64].

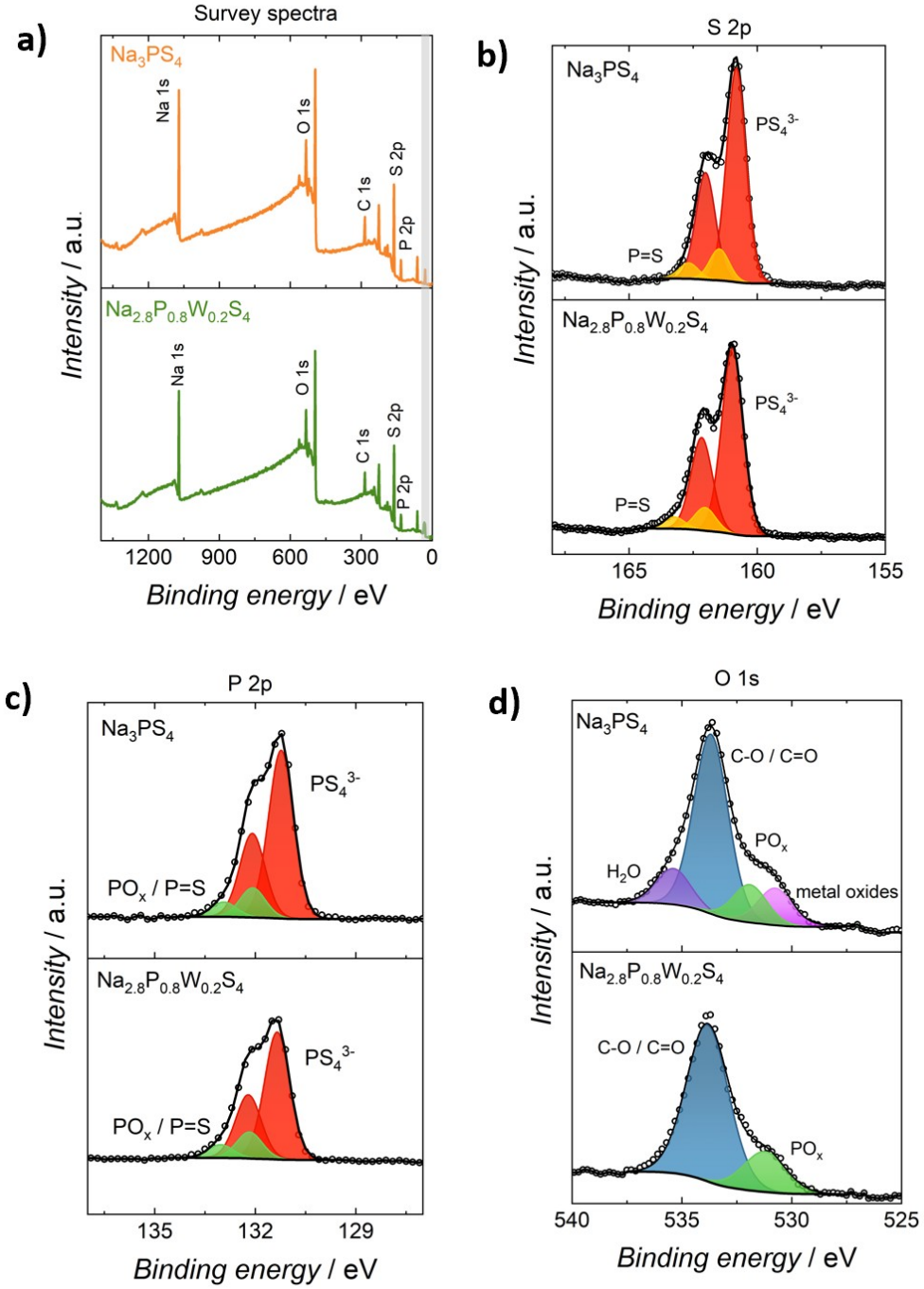

Figure 17: a) Survey spectra of Na_3PS_4 and $Na_{2.8}P_{0.8}W_{0.2}S_4$, the gray region shows the presence of W4f peaks that partially overlap with Na2p peaks. Detailed spectra of b) S2p, c) P2p, and d) O1s of both NPS and NPWS.

5.2 Composite cathodes with Na_3PS_4

To investigate the correlation between positive electrode microstructure and electrochemical performance, two cathode composites (FeS_2 / Na_3PS_4 / car-

bon black) were prepared by ball milling with two different procedures. In particular, the composites were prepared using different weight ratios between the milling media and the sample. For the soft milled composite (NPS SM), the weight ratio between the ZrO_2 milling medium and the sample was 10:1, while for the hard milled composites (NPS HM) a 20:1 media-to-sample ratio was used. The milling procedures employed for these composites are softer than the procedures used for pyrite-based Li-S composite, because of the higher ionic conductivity of the SE used for Li batteries (8 mS cm^{-1} for $LPSCl_{1.5}$ and 0.17 mS cm^{-1} for NPS). To ensure that the milling procedure did not lead to any unwanted side reaction and to exclude contamination, XRD and XPS were employed. Figure 18 shows the diffraction patterns of the solid electrolytes and cathode composites, as well as FeS_2. It was not possible to detect the carbon black contribution in the diffraction patterns because of its amorphous nature.

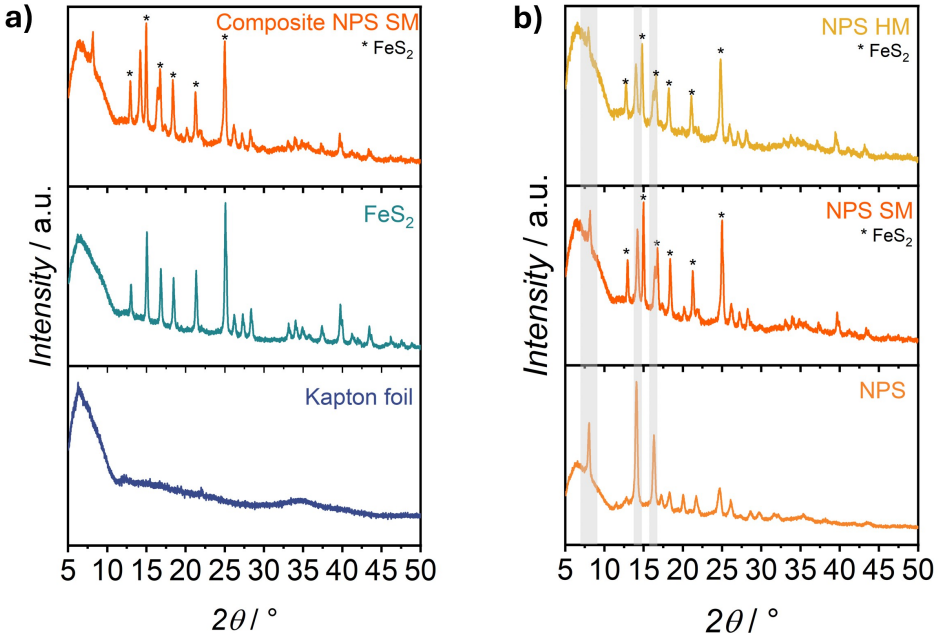

Figure 18: a) Diffraction patterns of the soft-milled cathode composite (NPS SM) and those of FeS_2 and kapton foil as a reference. b) Comparison between the diffraction pattern of the solid electrolyte (NPS) and both soft-milled (NPS SM) and hard-milled (NPS HM) cathode composites.

All the diffraction patterns show a wide reflection appearing between 5 and 10°, this is attributed to the kapton foil that is used to avoid air

exposure during the measurements. Figure 18a shows a comparison between the diffraction patterns of FeS_2 and one of the cathode composites. From this it can be seen that there is no significant loss of crystallinity of FeS_2 after ball milling. This is in line with the high Mohs hardness (6-6.5) of pyrite [60]. Figure 18b shows the comparison between the solid electrolyte (NPS) and the two cathode composites (NPS SM and NPS HM). The most intense reflections of the solid electrolyte are highlighted in gray. This comparison shows that the intensity of the SE reflections is decreasing when using harder milling procedures. This could be due to a decrease in crystallinity induced by ball milling and might lead to a loss of ionic conductivity of the solid electrolyte. In any case, all reflections present in the diffraction patterns of the composites can be attributed to FeS_2 or SE, showing that there is no side reaction during the preparation of the composite. However, since XRD can detect only crystalline phases, XPS was employed to further exclude the presence of side products and contamination. Figure 19 shows the XP spectra of the two investigated cathode composites.

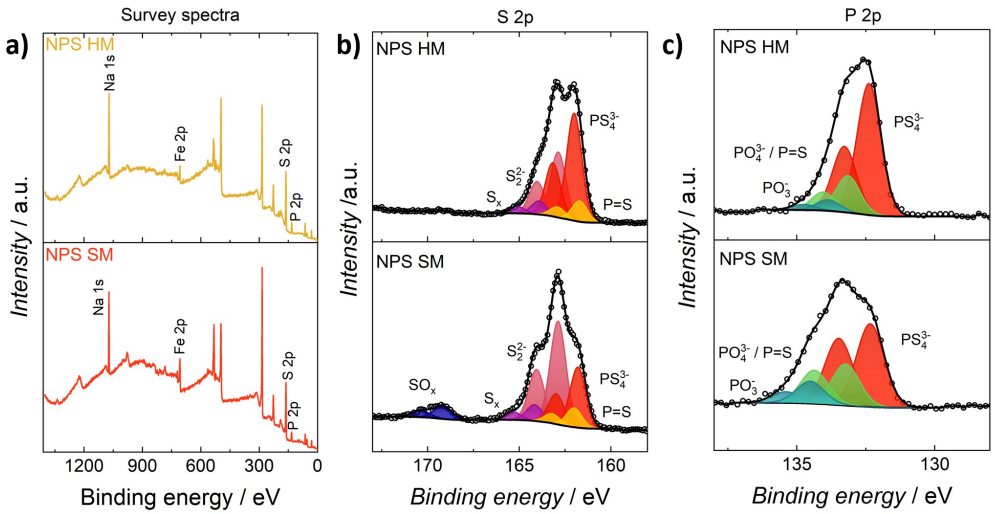

Figure 19: a) Survey spectra for both soft (NPS SM) and hard-milled (NPS HM) cathode composites. Detailed b) S2p and c) P2p spectra for both composites.

Figure 19a shows the survey spectra of the analyzed samples. From them the presence of FeS_2 and Na_3PS_4 can be seen (Na1s, Fe2p, S2p, and P2p peaks are labeled). Additionally, the detailed spectra of S2p and P2p

are shown (Fig. 19b and c). From the comparison between the detailed spectra shown in Figure 19b and c and those of the solid electrolyte (Fig. 17) it can be seen that there is a shift in the binding energies for the composites. This shift could be due to surface charging effects. In fact, sometimes the positive charge resulting from the emission of a photoelectron is not well compensated, leading to a shift of the peaks to higher binding energies [65]. This normally happens in the battery field because of the inhomogeneity of the samples. The S2p spectra show the two doublet peaks of the solid electrolyte (PS_4^{3-} and P=S) as well as a doublet that could be attributed to the presence of FeS_2 (S_2^{2-}). Furthermore, the XP spectra for the soft milled composite show the formation of SO_x species (i.e. SO_4^{3-}) which is probably due to the storage of the composite. Therefore, both XRD and XPS data shows that there is no significant contamination in the composites that could affect the electrochemical performance of the cells.

Consequently, the prepared composites were used as positive electrodes in half-cell setups with Na-Sn (negative electrode) and Na_3PS_4 (separator). Figure 20 shows the cycling performance of these cells.

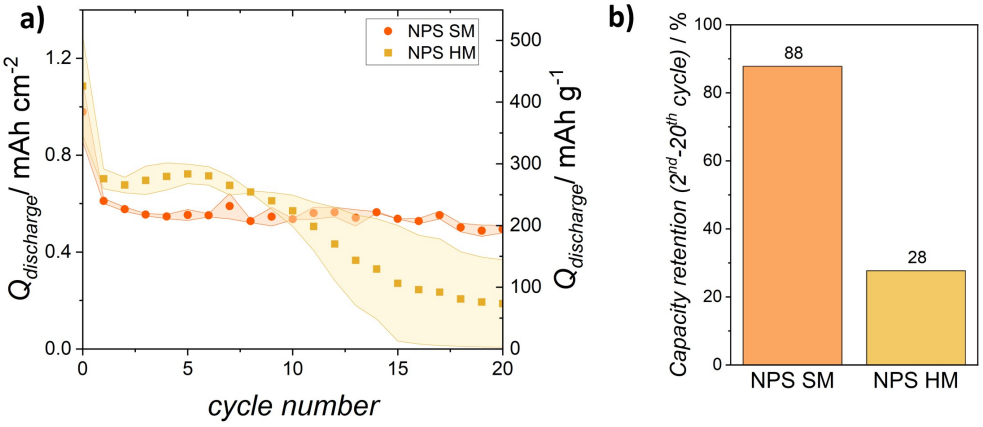

Figure 20: a) Discharge capacity *vs.* cycle number plots for Na-Sn A |Na_3PS4 |NPS SM and Na-Sn A |Na_3PS4 |NPS HM cells, and b) their capacity retentions. The capacity retentions were calculated between the 2^{nd} and the 20^{th} cycle.

The cycling curves show that initially higher capacities are achieved with the hard-milled composite. This could be due to the smaller particle size for the NPS HM composite, which could lead to more effective CAM utilization.

The high deviation observed in the cycling curves for cells with the NPS HM composite is due to the fact that one cell short-circuited after 15 cycles. However, both cells with the hard-milled composite show a marked decrease in capacity after only 10 cycles that leads to inadequate capacity retentions (only 28 % of capacity retained after 20 cycles).

A possible explanation could be that better contact between the particles can lead to additional degradation of the solid electrolyte inside the composites, which is reflected in the capacity retentions. To better understand this behavior, SEM was employed to analyze the cross section of the cathode composites. The average particle size of 100 particles was evaluated using the software *ImageJ* and the results are shown in Figure 21b and d. A log-normal distribution was used to describe the size of the particles within the composites, because it is particularly suitable to represent positive quantities (such as particle size, energies, and concentrations) [66].

The size of the particles inside the composites differs from the particle size measured for the solid electrolytes (Fig. 16), this could be due to several factors. First, the average particle size of the composites was evaluated by taking into account the size of both SE and FeS_2. Second, smaller particles are harder to measure with the software *ImageJ* and only 100 particles were considered. Lastly, to measure the particles in the particle size analyzer, the SEs had to first be dispersed in a solvent (mixture of xylene and oppanol). Therefore, the larger particles tend to precipitate faster while smaller tend to aggregate, leading to an inexact estimation of the particle size. In any case, Figure 21 shows a decrease in particle size for the hard-milled composite. Although this can effectively explain the higher capacities achieved with NPS HM, the difference in capacity retentions is not as clear. In fact, the size of the particles inside the hard-milled composites is still high. Therefore, in the case of the hard-milled composite, the anode might play an important role in the decreasing capacities.

To further investigate the cell performance, partial ionic and electronic conductivities of the composites were determined using DC measurements. To do this, a constant voltage was applied and the current response was

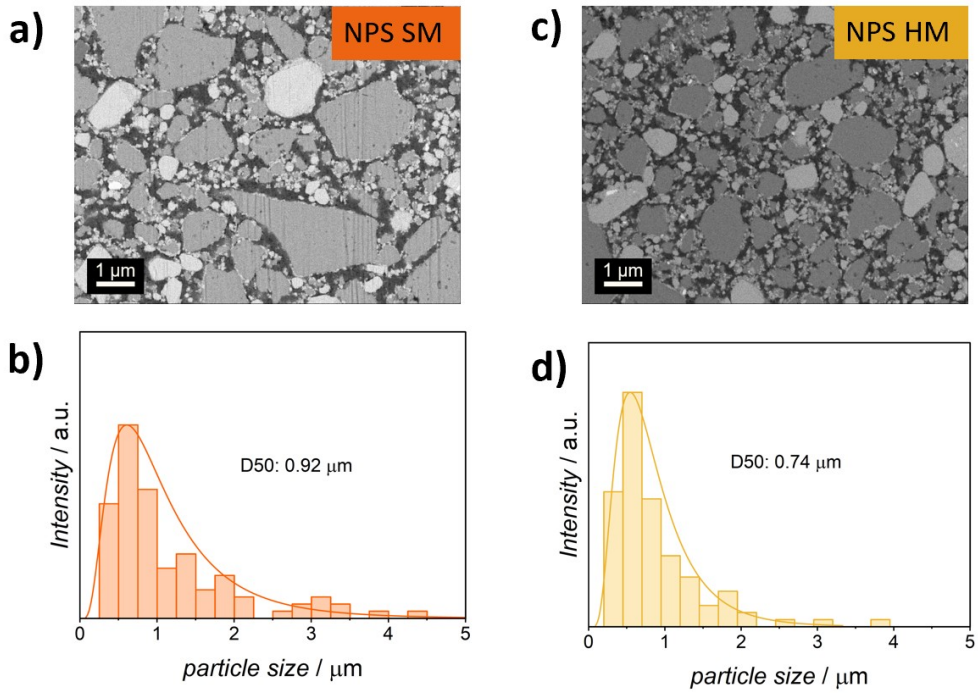

Figure 21: a) SEM image of the cross section of the soft-milled cathode composite (NPS SM) and c) the hard-milled composite (NPS HM). The images were taken with an ESB detector at the same magnification. The ESB detector allows to differentiate the components that are present in the composite based on their mass. In a) and c) the black areas are carbon black, the solid electrolyte is dark gray and FeS_2 is light gray. b) and d) average particle size of the composites evaluated with the software *ImageJ*.

recorded. The slope of i *vs.* U the plot gives the electronic and ionic resistance from which the conductivities can be calculated (Eq. 16). For electronic conductivities, the experimentally determined resistance is directly the electronic resistance of the setup. To calculate the ionic conductivities, the resistance of the SE and the interface between SE and Na-Sn had to be evaluated. Impedance spectroscopy was employed to estimate the resistance. In particular, impedance spectra of a symmetric cell made of SE and anode (Na-Sn |Na_3PS_4 |Na-Sn) were recorded and fitted to evaluate the resistance. Figure 22 shows the voltage steps applied during the DC measurements and the current recorded, as well as EIS evolution during 17 h and the fit performed on the first recorded spectrum.

Table 6 shows the calculated ionic and electronic conductivities of the investigated composites, as well as the ionic conductivity of the solid elec-

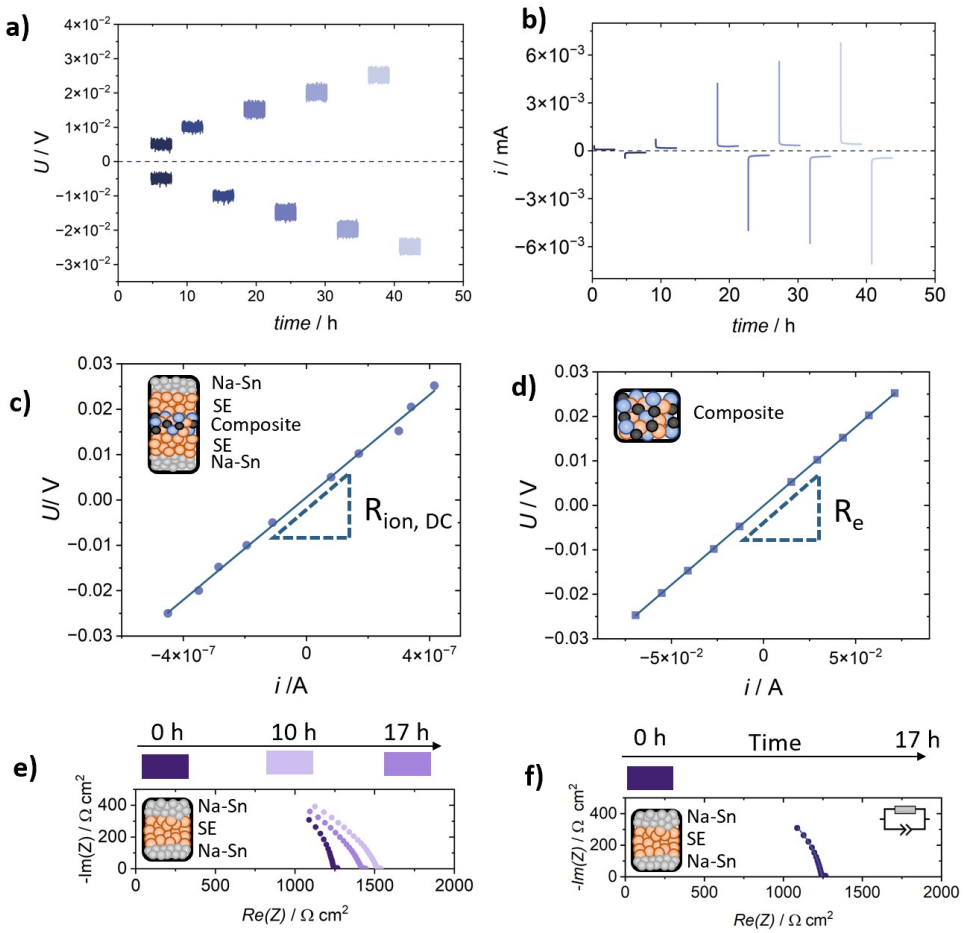

Figure 22: a) Voltage steps applied during the DC procedure and b) the current response. The same steps are applied for both ion and electron blocking setups. Setup used for evaluating ionic (c) and electronic conductivities (d), and ionic and electronic resistances evaluated from i *vs.* U plots. e) EIS evolution for a symmetric cell Na-Sn $|Na_3PS_4|$Na-Sn. f) Fit of the impedance spectra recorded right after attaching the cell.

trolyte, for comparison.

Table 6: Ionic and electronic conductivities for the SE and the soft-milled (NPS SM) and hard-milled (NPS HM) cathode composites.

Material	**Ionic conductivity** (mS cm^{-1})	**Electronic conductivity** (mS cm^{-1})
NPS	0.17	-
NPS SM	$5 \cdot 10^{-3}$	$2 \cdot 10^{3}$
NPS HM	$2 \cdot 10^{-2}$	10^{3}

Measurements for both the ionic and electronic conductivities were performed once. Because of this and the intrinsic errors in the evaluation of the

thickness of the samples, these measurements give a rough estimation of the conductivities. Further analysis has to be performed to effectively assess the conductivities of the composites employing both DC and AC methods. The ionic conductivity of the composites is several orders of magnitude lower than the electronic conductivity. The high electronic conductivities could be due to the well-connected carbon domains that surround the SE particles (Figure 21) [60]. However, the low ionic conductivities show that Na^+ diffusion inside the composites plays a key role on the cell performance. Furthermore, the ionic conductivities of the composites are one order of magnitude lower than the conductivity of the SE (Table 6), thus showing that milling leads to a loss of ionic conductivity.

In conclusion, it has been shown that microstructure plays an important role on cell performance, and, in particular, smaller particles inside the composites lead to higher capacities. However, since both microstructure and high ionic conductivities are expected to be decisive for cell performance [61], Na_3PS_4 was substituted with the more ionic conductive $Na_{2.8}P_{0.8}W_{0.2}S_4$ in the cathode composites and the relationship between particle size and cell performance was also investigated.

5.3 Composite cathodes with $\mathbf{Na_{2.8}P_{0.8}W_{0.2}S_4}$

To effectively enhance Na^+ diffusion inside the positive electrode, $Na_{2.8}P_{0.8}W_{0.2}S_4$ (σ_{Na^+}= 14.7 mS cm^{-1}) was used as a catholyte instead of Na_3PS_4. Different composites (FeS_2 / $Na_{2.8}P_{0.8}W_{0.2}S_4$ / CB) were prepared with two milling procedures. As before, soft-milled (media-to-sample ratio 10:1) and hard-milled (media-to sample ratio 20:1) cathode composites were prepared. For simplicity, the soft-milled composite will be called NPWS SM, while the hard-milled one NPWS HM.

First, both XRD and XPS were employed to ensure that the milling process did not lead to unwanted side reactions. Figure 23b shows a comparison between the diffraction patterns of the solid electrolyte (NPWS) and the prepared cathode composites (NPWS SM and NPWS HM).

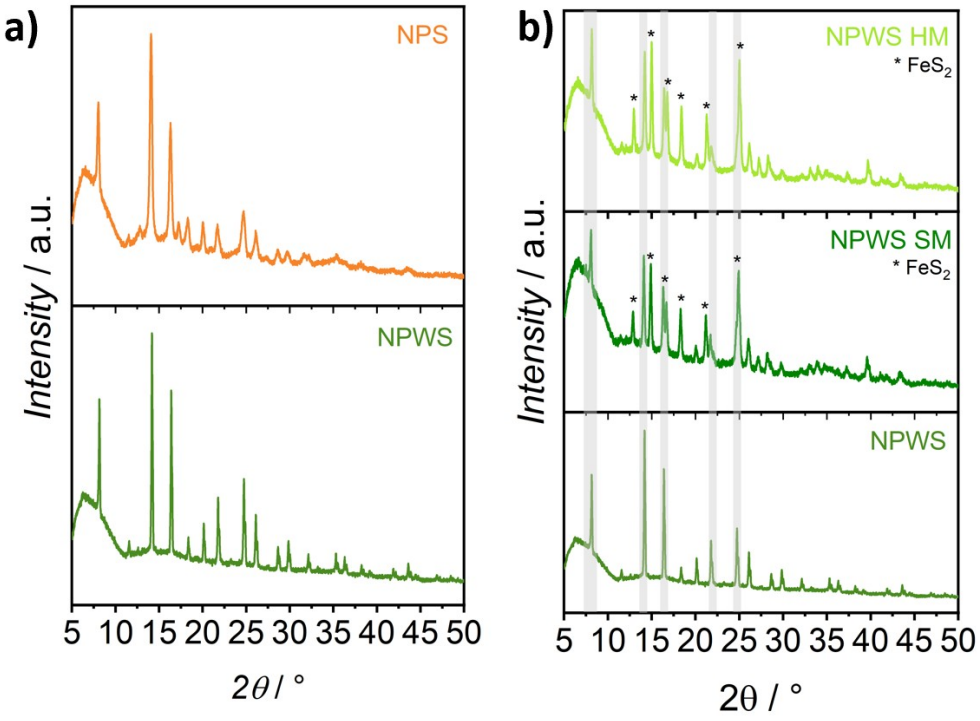

Figure 23: a) Comparsion bewteen the diffraction patterns of the solid electrolytes (NPS and NPWS). b) Diffraction patterns of the solid electrolyte (NPWS), as well as those of the soft-milled (NPWS SM) and hard-milled (NPWS HM) cathode composites.

In Figure 23b the most intense reflections of both FeS_2 and the SE are highlighted. Compared to Na_3PS_4, $Na_{2.8}P_{0.8}W_{0.2}S_4$ shows a higher crystallinity (Fig. 23a), which, however, is in part reduced in the cathode composites, probably due to the milling procedures. To further study the composition of the positive electrodes, X-ray photoelectron spectroscopy was employed. Figure 24 shows the survey spectra and the detailed spectra of S2p and P2p for both the soft- and hard- milled composites.

The survey spectra (Fig. 24a) show the presence of both FeS_2 (Fe2p and S2p peaks) and the solid electrolyte (Na1s, S2p, P2p and W4f peaks). The fits of the S2p and P2p spectra are shown in Figure 24b and c. The S2p envelope shows contributions from both FeS_2 (S_2^{2-}) and $Na_{2.8}P_{0.8}W_{0.2}S_4$ (PS_4^{3-} and P=S), while the P2p peak shows the possible presence of phosphates (PO_4^{3-} and PO_3^{-}). From the XRD and XPS analysis, it can be concluded that the milling procedures did not lead to unwanted side re-

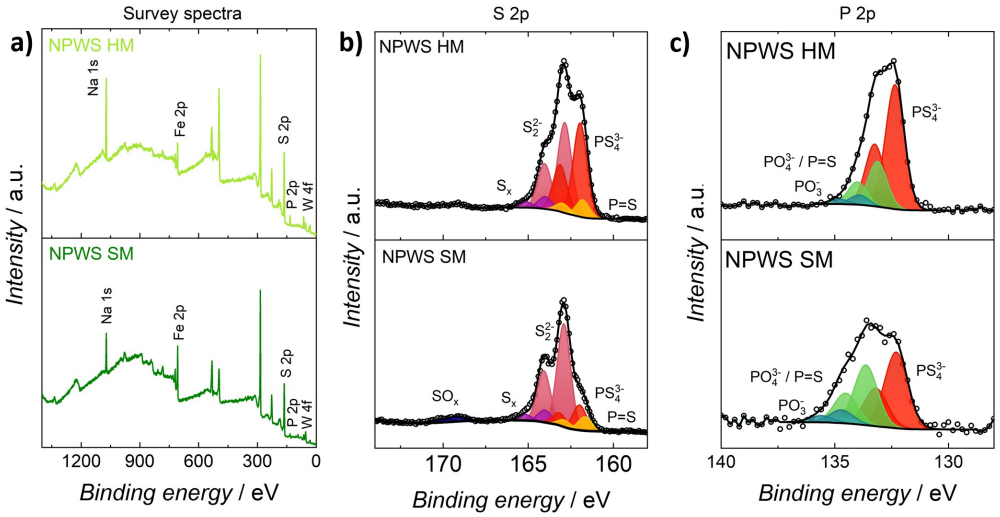

Figure 24: a) Survey spectra of the two cathode composites (NPWS SM, NPWS HM). Detailed b) S2p and c) P2p spectra for both soft- and hard-milled composites.

actions. Furthermore, no significant contamination could be detected by XPS.

Subsequently, the two prepared composites were used as positive electrodes in pyrite-based Na-S SSBs with Na-Sn as the negative electrode and Na_3PS_4 as separator. Na_3PS_4 was used as a separator because of the instability of $Na_{2.8}P_{0.8}W_{0.2}S_4$ in contact with the Na-Sn anode. The discharge curves and capacity retentions for these cells are shown in Figure 25a and 25b.

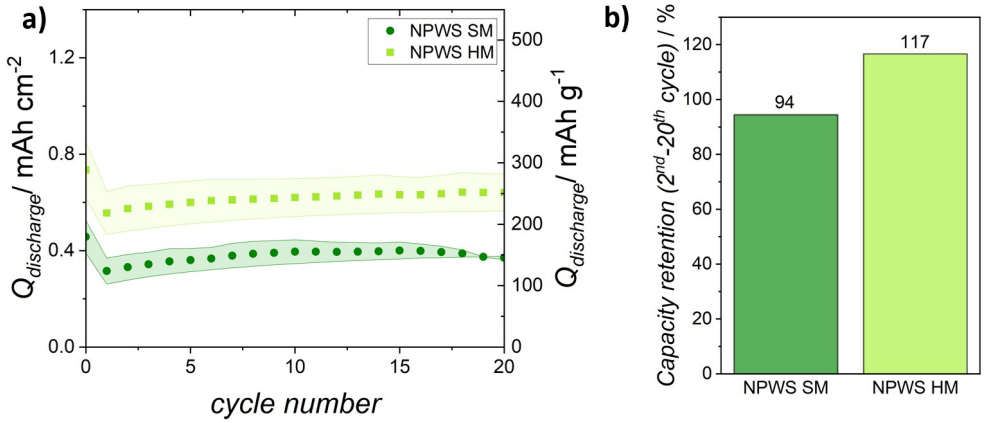

Figure 25: a) Discharge capacity *vs.* cycle number plot and b) capacity retentions for Na-Sn |NPS |NPWS SM and Na-Sn |NPS |NPWS HM cells.

First, it can be observed that cells with hard-milled composites achieve significantly higher capacities than cells with soft-milled composites (cells with NPWS HM show an increase of approximately 100 mAh g^{-1} compared to NPWS SM cells). This can be ascribed once again to the smaller particle size achieved with the hard-milled composites that increase the contact between the different components inside the composites. Figure 26 shows SEM images of the cross sections of the cathode composites (NPWS SM, NPWS HM) as well as their particle size distribution. The SEM images were taken with an ESB detector that allows to differentiate between elements based on their mass. However, in this case, it is not possible to differentiate between FeS_2 and the SE.

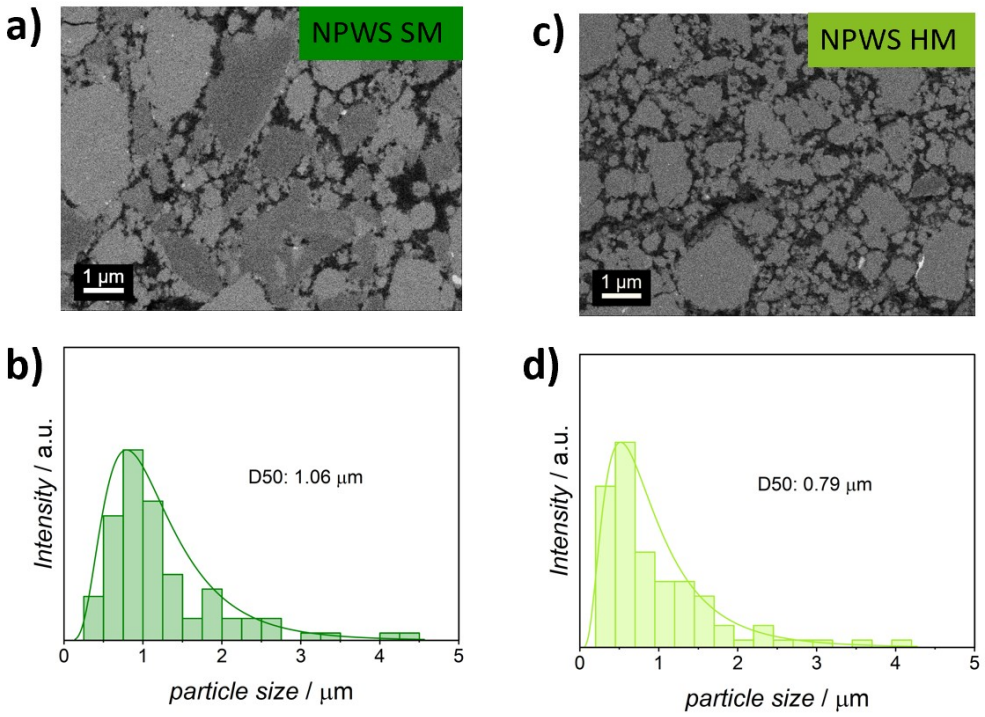

Figure 26: a) SEM image of the cross section of the soft-milled cathode composite (NPWS SM) and c) the hard-milled composite (NPWS HM). The images were taken with an ESB detector at the same magnification. b) and d)particle size distribution of the composites evaluated with the software *ImageJ*.

The harder milling procedures were effective in reducing the size of the particles within the composites, reflecting the cell performance. However, it is not clear whether the larger particles still present in the composites are

FeS_2 or SE particles. To distinguish the chemical composition, EDS maps were used (Fig. 27). The presence of FeS_2, NPWS, and carbon black are confirmed by the Fe, Na, and C maps in Figure 27, respectively.

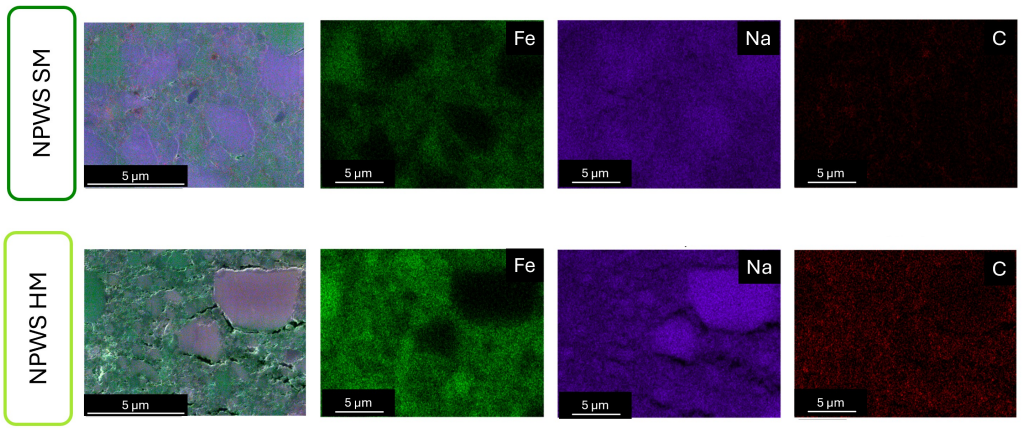

Figure 27: Top: EDS of the soft-milled composite with elemental map distribution. Bottom: EDS of the hard-milled composite. The elemental maps show the distribution of the different components inside the composites. FeS_2 is shown in green (Fe), $Na_{2.8}P_{0.8}W_{0.2}S_4$ in purple (Na map) and carbon black in red (C).

From the EDS maps it can be clearly seen that both the cathode active material and the SE still have large particle size inside the composites. In fact, even though the hard-milled composite does not show a large decrease in particle size, it still has a significant effect on cell performance. This highlights the importance of having good contact between the particles and suggests that further reducing the particle size (with even harder milling procedures) might lead to even higher capacities. In fact, previous studies on FeS_2-based Li-S SSBs show that higher capacities are obtained with composites that have submicrometer FeS_2 particles confined in an homogeneous matrix of SE [60].

However, the cells with the NPWS composites achieve capacities similar to those of the cells with the NPS composites (200 / 250 mAh g^{-1}). To better understand this behavior, the ionic conductivity of the NPWS composites was calculated, and the results are shown in Table 7.

It was not possible to obtain the ionic conductivity of the NPWS SM composite because the i *vs.* U plots did not show a linear behavior. There-

Table 7: Ionic and electronic conductivities for the solid electrolyte (NPWS), soft-milled (NPWS SM), and hard-milled (NPWS HM) cathode composites.

Composite	**Ionic conductivity** (mS cm^{-1})	**Electronic conductivity** (mS cm^{-1})
NPWS	14.7	-
NPWS SM	-	$2 \cdot 10^{3}$
NPWS HM	$5 \cdot 10^{-3}$	10^{3}

fore, to assess the ionic conductivity of this composite, AC methods should be employed. Composites with W-doped NPS show conductivities similar to those of the NPS composites. These results suggest that the initially higher ionic conductivity of $Na_{2.8}P_{0.8}W_{0.2}S_4$ is substantially decreased due to ball milling.

To investigate whether the loss in conductivity observed for the composites studied in this work is in line with what observed for other systems, the results obtained in this thesis were compared with other works. Figure 28 shows a comparison between the ionic conductivities of the SEs and cathode composites for different CAMs.

The preparation of cathode composites by ball milling intrinsically reduces the ionic conductivity of the solid electrolytes. In fact, in the case of LPSCl, 62 % of the ionic conductivity is lost after ball milling (Fig. 28) [40]. Furthermore, when carbon and CAM are added, the overall ionic conductivity of the composites additionally decreases. Ohno *et al.* studied the effect of adding different carbon black percentages to a SE / CB cathode composite [40]. In this study, they show that increasing the carbon content inside the composites strongly reduces ionic conductivity (only 26% of conductivity retained with 10% carbon content), suggesting that microstructure has a relevant influence on ionic conductivity [40].

The results obtained in this work are in line with the results obtained for the other analyzed systems. However, it is worth noting that in the case of the NPWS composites almost all of the ionic conductivity of the SE is lost after ball milling. Therefore, cells with NPS and NPWS composites

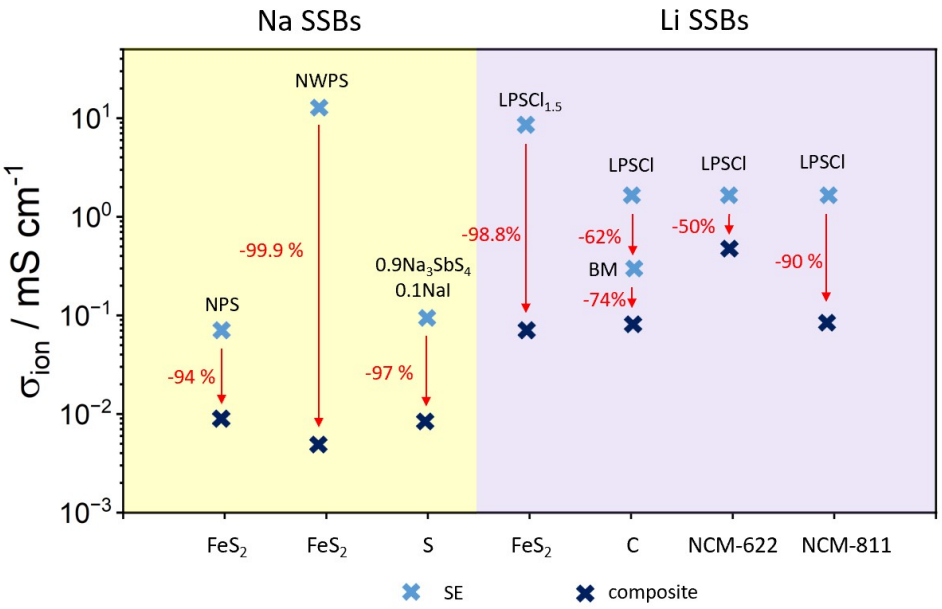

Figure 28: Ionic conductivities of different solid electrolytes and those of the ball-milled cathode composites prepared with those SEs and the labeled CAMs. Left: comparison between the ionic conductivities calculated in this work and those calculated by Wan *et al.* [67] for Na SSBs. Right: comparison between the ionic conductivities of SE and composites for various cathode active materials. Adapted from [40, 60, 61, 62].

show comparable capacities. To explain the considerable loss of conductivity observed for NPWS, a greater knowledge of the properties of the solid electrolyte (e.g. hardness) is needed, however, this goes beyond the aim of this work.

However, the capacity retentions of cells with NPWS composites (Fig. 25b) are considerably different from those of the cells with NPS composites (Fig. 20b). Specifically, cells with W-doped NPS as the catholyte show improved retentions. This behavior has already been observed by Shen *et al.* for all-solid-state lithium sulfur batteries [68]. A possible explanation for this behavior lies in the formation of WS_2 at the interphase between the active material and the catholyte. In fact, WS_2 is a mixed ionic and electronic conductor that could facilitate electron and ion transport within the interphase, therefore stabilizing the interphase reactions [68]. Furthermore, since WS_2 is redox active, it could facilitate the sulfur (FeS_2) redox

in the interphase, thus enhancing conversion kinetics and improving its reversibility [68]. Therefore, in the case of NPWS composites the possible formation of insulating products that could affect cell performance might be mitigated. The formation of WS_2 for pyrite-based Na-S SSBs still has to be investigated. To do this, techniques such as XPS and TOF-SIMS could be employed.

Although cells with NPWS as catholyte do not show the expected increase in capacity due to the higher ionic conductivity of NPWS, they still display capacities similar to those of cells with NPS composites while showing significantly improved capacity retentions. Because of this, the hard-milled NPWS composite was used for the experiments that will be discussed in the following chapter.

6 Sodium Iodide as an additive

6.1 Electrochemical characterization

This work focuses on understanding whether I_2 can be formed from NaI under the chosen cycling conditions and, eventually, whether it can mediate the oxidation of the chemical species present during cycling to enhance cycling stability and rate capability. However, it is not yet clear which chemical species are produced during cycling in pyrite-based solid-state Na-S batteries. In fact, while there are several reports on the reactions occurring in pyrite-based Li-S solid-state batteries, up to now, no study has reported on the reactions in pyrite-based Na-S SSBs.

Studies on FeS_2-based Li SSBs report the formation of FeS, Li_2S and Fe^0 during first discharge (Eqs. 21) [60, 69].

$$FeS_2 + 2Li^+ + 2e^- \rightarrow FeS + Li_2S \rightarrow Fe^0 + 2Li_2S \tag{21}$$

Therefore, assuming the same mechanism for FeS_2-based Na-S SSBs, equation 21 can be rewritten as follows:

$$FeS_2 + 2Na^+ + 2e^- \rightarrow FeS^* + Na_2S^* \rightarrow Fe^{0*} + 2Na_2S^* \tag{22}$$

The formation of the species labeled with an asterisk in Eq. 22 has not yet been reported. In fact, studies on Na-S solid-state batteries reported the formation of a wide range of polysufides during discharge, such as Na_2S_5, Na_2S_4, Na_2S_2, and Na_2S, as well as high-order polysufides (Na_2S_x with x=6-8) [70]. Therefore, the reaction mechanism for FeS_2-based Na-S SSBs could be more complicated than is assumed in this work.

On the other hand, the redox reactions of NaI have previously been studied for sodium ion batteries and are summarized in equations 23 and 24 [71]. During charging, NaI is oxidized to NaI_3 which is subsequently oxidized to I_2. During discharging the inverse process is observed [71].

$$3NaI \rightleftharpoons NaI_3 + 2Na + +2e^- \tag{23}$$

$$2NaI_3 \rightleftharpoons 3I_2 + 2Na^+ + 2e^- \tag{24}$$

The overall redox reaction of NaI is summarized in eq. 25.

$$2NaI \rightleftharpoons I_2 + 2Na^+ + 2e^- \tag{25}$$

To study the redox-mediating effect of iodine, cathode composites with different NaI contents were prepared. In particular, three composites with increasing NaI content were tested, the first composite was prepared by mixing FeS_2, NPWS and CB (volume fractions 27 %, 55 % and 18 %, respectively) with hard-milling procedures (NPWS HM). The other composites were prepared by substituting different fractions of the solid electrolyte with NaI. Specifically, composites with 5 % volume fraction of NaI (NaI 5 %), and 15 % of NaI (NaI 15 %) were tested. Figure 29 shows the volume (a) and mass (b) fractions of the different materials inside the cathode composites.

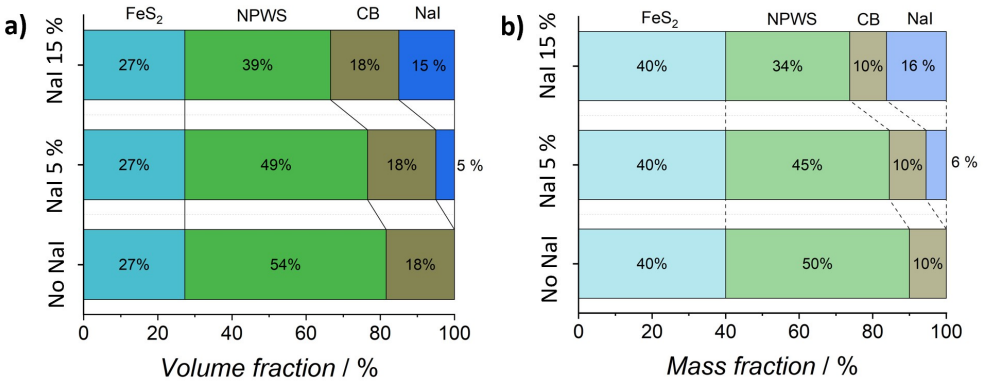

Figure 29: a) Volume fractions of the different materials (FeS_2, SE, CB, and NaI) for the three analyzed composites (No NaI, NaI 5 %, and NaI 15 %). b) Mass fractions for the materials in the same composites.

On the basis of thermodynamic calculations, the reaction described in eq. 25 is expected to occur at 2.96 V *vs.* Na / Na^+. The potential of the anode used (Na-Sn) was assessed to be 0.62 mV *vs.* Na / Na^+. Therefore,

to effectively trigger the formation of I_2, all cells were cycled between 0.5 and 3.2 V *vs.* Na-Sn. Figure 30 shows the discharge curves for cells with the three different cathode composites: without NaI (No NaI), with 5 % in volume of NaI (NaI 5 %), and with 15 % in volume of NaI (NaI 15 %).

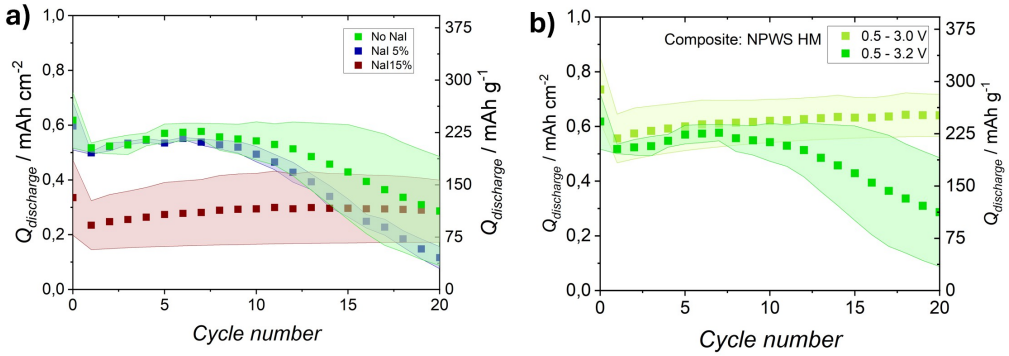

Figure 30: a) Discharge capacity *vs.* cycle number plots for cells with composites without NaI (no NaI), with 5 % in volume of NaI (NaI 5 %), and 15 % in volume of NaI (NaI 15 %). b) Comparison between Na-Sn |NPWS |FeS_2 / NPWS / CB cells cycled with two different higher cutoff potentials: 3.0 and 3.2 V *vs.* Na-Sn.

The composite NaI 15 % shows significantly lower initial capacities compared to the other composites. This could be due to a decrease in the ionic conductivity of the composite due to its lower amount of SE (38 % in volume of SE inside the composite). Therefore, for further analysis, only the the composites without (No NaI) and with 5 % in volume of NaI (NaI 5 %) will be considered.

From Figure 30b it can be seen that cells cycled between 0.5 and 3.2 V show a sharp decrease in capacities compared to cells cycled up to 3.0 V. Moreover, no substantial difference can be detected between the cycling curves of cells with and without NaI. Therefore, to investigate this behavior, cyclic voltammetry and differential capacity plots were employed, Figure 31 shows a comparison between them.

The differential capacities were calculated from the charge / discharge curves of cells cycled at 0.1 C, while the scan rate used for the cyclic voltammetry was 0.05 mV / s. Both dQ / dU plots and CVs show the appearance of a reduction peak around 0.8 V during the first discharge. This peak

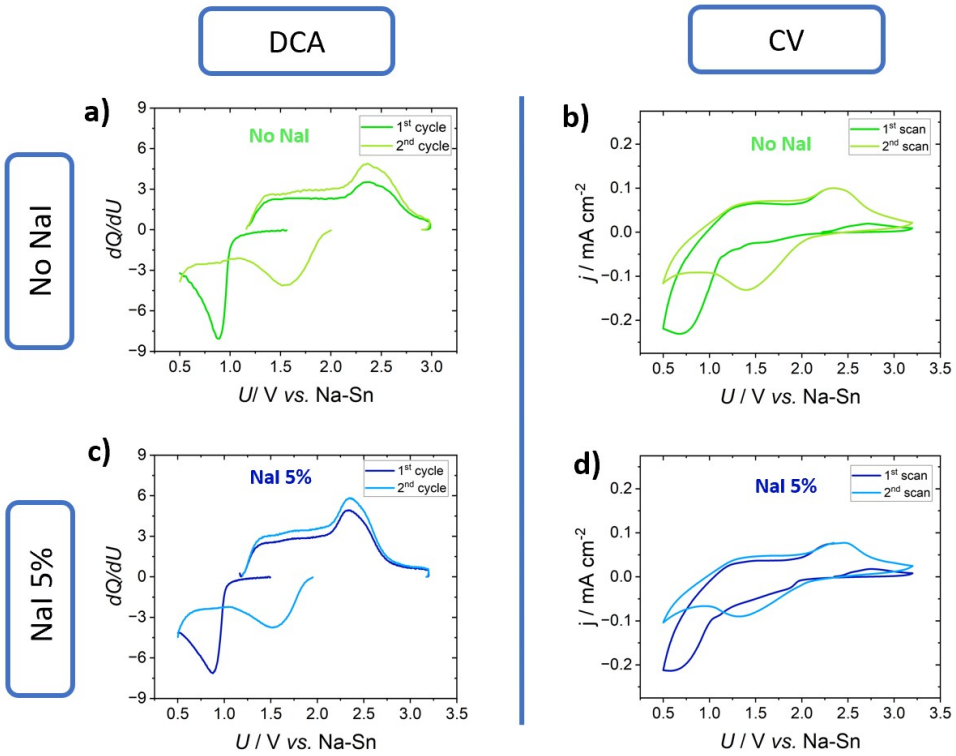

Figure 31: Differential capacity plots and cyclic voltammetries for cells without NaI (a,b) and (c,d) with 5 % NaI in the composites.

might be attributed to the first irreversible reaction of FeS_2 that is reported for pyrite-based Li-S SSBs [60, 69]. During the second discharge, a peak around 1.5 V emerges and can be attributed to electrolyte decomposition [26]. The peak-to-peak separation (ΔE_p) in both CVs is approximately 1 V, suggesting that the reduction process may not be fully reversible [72]. Therefore, the worse cycling stabilities shown in Figure 30 could be due to irreversible decomposition of the solid electrolyte at higher potentials. However, no difference could be detected between the differential capacity plots and the CVs for the cells with and without NaI. Therefore, to assess the formation of I_2, cells were charged at lower C-rates (0.02 C and 0.05 C) and discharged at a constant rate of 0.1 C; both at room temperature (25 ° C) and at 60 ° C (Fig. 32). This was done to improve the reaction kinetics. In fact, at lower C-rates reactions inside the composites have more time to occur, while higher temperatures enhance the reaction rate.

Figure 32 shows a second oxidation peak appearing around 1.2 V for

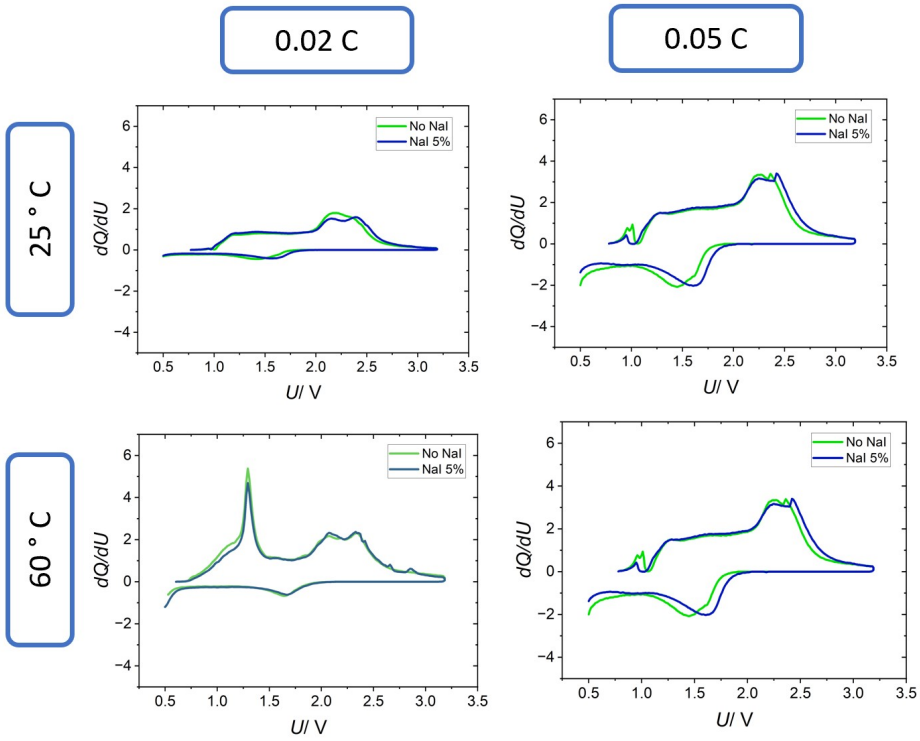

Figure 32: Differential capacity plots for cells without NaI and with 5 % NaI in the cathode composites. The cells were charged at 0.02 and 0.05 C and discharged at 0.1 C at 25 ° C and 60 ° C. The plots for the first discharge are not shown.

the cells cycled at 60 ° C. Although it is not clear whether this is due to electrolyte degradation or to any other reaction, since this peak is present for both the cells with and without NaI, it cannot be ascribed to the oxidation of NaI. In fact, there is no detectable difference between the cells with and without NaI in the composites. For this reason, XRD and SEM analyses were performed to detect any changes inside the composites and better understand the electrochemical performance of the cells.

6.2 Analytical characterization

To better understand the electrochemical performance of the cells containing NaI, XRD and SEM were employed. Specifically, the diffraction patterns of the pristine composites were recorded to ensure that the preparation of the composites did not produce any unwanted side product that might affect cell performance. Figure 33 shows a comparison between the diffraction patterns of NaI and the two composites with NaI (NaI 5 % and NaI 15 %). The diffraction pattern of the composite without NaI (NPWS HM, No NaI) was shown in Figure 23.

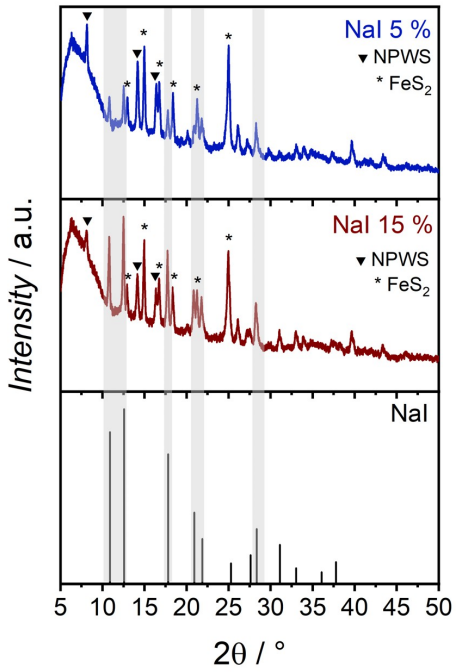

Figure 33: Diffraction patterns of the two composites with NaI (NaI 5 % and NaI 15 %) as well as the diffraction pattern of NaI as a reference [73].

The XRD patterns show the presence of FeS_2, NPWS, and NaI (grey regions). As expected, the reflections of NaI in the composite NaI 5 % are less intense than in the composite NaI 15 % due to its lower amount.

Furthermore, to better understand the electrochemical performance of the cells with NaI 5 % composites, SEM-EDS images of cross section of the pristine composite and after first discharge / charge were taken. Figure 34 shows the SEM-EDS images of the pristine cross section of the cathode

composite with 5 % in volume of NaI.

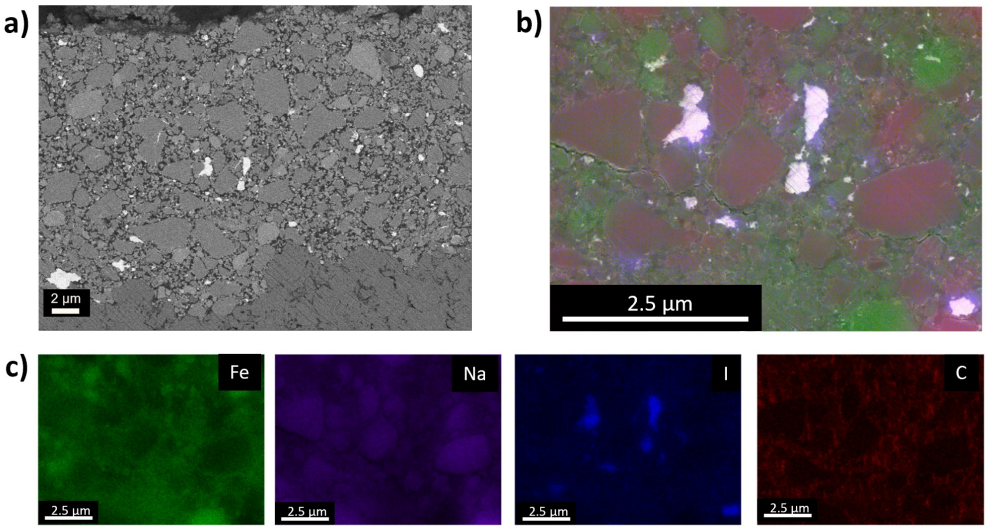

Figure 34: a) Pristine cross section of FeS_2 / NPWS / CB / NaI 15 % cathode composite, taken with an ESB detector. b) and c) EDS maps of the pristine cross section of the NaI 5 % cathode composite. The element maps show the presence of FeS_2 (Fe map, in green), NPWS (Na map, in purple), carbon black (C map, in red) and NaI (I map, in blue).

The SEM image in Figure 34a shows the presence of brighter spots that were not present in the composite without NaI (Fig. 26). The EDS maps (Figure 34b and c) confirm that the white spots can be attributed to NaI. However, the SEM images reveal that sodium iodide is highly inhomogeneously distributed. In fact, inside the composite there are spots in which NaI is not present and areas in which NaI with particle size exceeding 2 μm is detected. This might explain the electrochemical behavior. Indeed, because of the low amount and inhomogeneous distribution of NaI, the redox mediating effect of iodine might not be detected. However, the question of whether I_2 is formed during cell charging remains, although it was not electrochemically detected. To evaluate the possible formation of iodine, a cell was discharged and then charged at 0.02 C at 60 ° C, after charging the potential of the cell was held for 48 h and the cross section of the cathode was analyzed with SEM-EDS. The SEM-EDS image of the cross section of the composite (NaI 5 %) after discharge / charge are shown in Figure 35, in which Figs. 35b and c are zoomed in images of the NaI spot shown

in Figure 35a. XPS analysis was performed on the sample after charge / discharge, however, the presence of I_2 could not be detected, possibly due to oxidation of the sample during preparation.

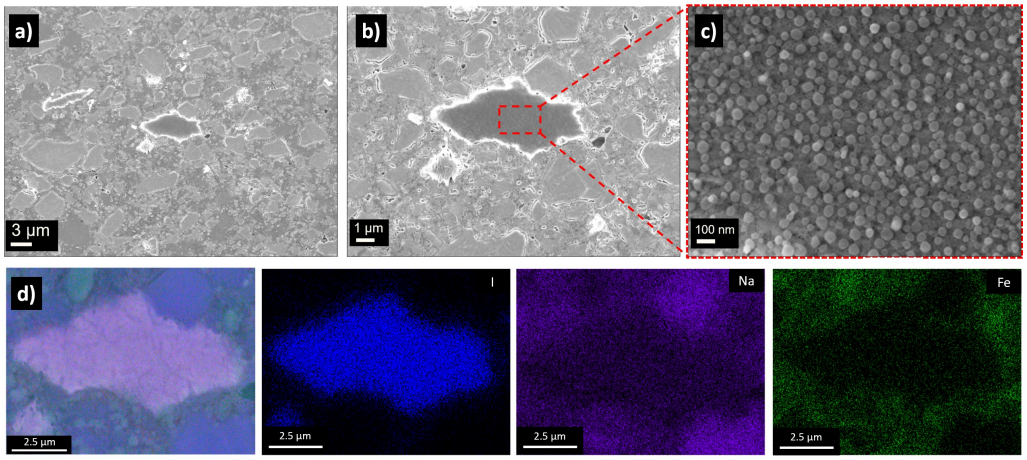

Figure 35: a) SEM images of the cross section of the composite NaI 5 % after discharge and then charge at 60 ° C. b) and c) zoomed in images of a). The images were taken with an Inlens detector at different magnifications. d) EDS maps of the same area analyzed with SEM, and elemental maps of iodine (blue), sodium (purple), and iron (green).

The SEM-EDS images show that a morphological change is happening inside the NaI particles. Specifically, the NaI particles after cycling appear darker compared to the pristine (Fig. 34). Additionally, a round-shaped morphology for the sodium iodide particles is observed at high magnifications in the cycled composite. The EDS maps of the composite after discharge / charge show the presence of an iodine-rich area surrounded by Na- and Fe-rich areas. This observation further suggests that a change is occurring inside the NaI particles; however, there is no clear evidence of whether I_2 or NaI_3 (I_3^-) is forming, because EDS cannot detect the chemical state of the analyzed species. In this regard, XPS could give information on the oxidation state of iodine.

This study suggests that the production of a composite with a higher content of iodine-containing species (for example, additives or SEs containing iodine) could be effective in observing the redox-mediating role of iodine. In fact, SEM-EDS suggests that morphological changes inside the NaI particles are happening; however, their effect on the cell performance remains

unclear. To further analyze the NaI behavior, other characterization methods such as XPS and TOF-SIMS are needed.

7 Conclusions

This work focused on the understanding of the intricate relationship between positive electrode microstructure and electrochemical cell performance. To do this, cathode composites with different SEs (Na_3PS_4 and $Na_{2.8}P_{0.8}W_{0.2}S_4$) were prepared using various ball milling procedures. In line with previous reports, this work showed that small and homogeneously distributed particles inside the composites are effective in achieving high capacities. As a matter of fact, smaller particles reduce particle mismatch, allow greater utilization of the cathode active material, and help mitigate volume changes. To ensure high conductivity inside the composites, NPS was substituted as a catholyte with the more ionic conductive NPWS. However, the ionic conductivity measurements performed on the cathodes show that the ball milling procedures used to produce the composites lead to a huge loss of ionic conductivity of the SE (99.9 % of conductivity loss). Therefore, the capacities achieved for the cells with the NPS and NPWS composites were comparable. To further study this behavior, a better understanding of the properties of the SEs used is needed; however, this is beyond the aim of this work. In any case, it was observed that tungsten-doped solid electrolytes can effectively enhance cycling stability. This is possibly due to the formation of WS_2 which could stabilize the interphase reactions. To prove this, further investigation is required.

This work highlights the importance of effectively tuning cathode microstructure and reveals the potential of achieving even higher capacities for FeS_2-based Na-S SSBs by further reducing particle size within the positive electrode. Moreover, it was shown that the interphase instability between the anode and the SE has an effect on cell performance. Therefore, to rule out any contribution from the negative electrode, a stable anode / separator interphase has to be found. A possible solution for this could be to replace the NPS separator with more stable and conducting SEs, such as $Na_2B_nH_n$ and $NaCB_{n-1}H_n$. This class of electrolytes is particularly suitable because of their reduction stability, and high ionic conductivity, however, due to

their high cost, they were not employed in this work.

In addition, investigation of NaI as a possible redox mediator was carried out. To do this, composites with different NaI contents were prepared and tested. However, probably because of the inhomogeneous distribution of NaI in the positive electrode, the redox mediating effect of iodine still remains unclear. In any case, SEM-EDS analysis performed on a cycled composite shows a morphological change of NaI within the composite, suggesting a chemical change.

In conclusion, to carry out further research on iodine as a redox mediator, a better understanding of the reactions that occur at the positive electrode is needed. Therefore, a detailed study of the positive electrode with different characterization techniques (e.g. XPS, TOF-SIMS) is required.

References

[1] Gaoran Li et al. “Revisiting the Role of Polysulfides in Lithium-Sulfur Batteries”. In: *Advanced materials (Deerfield Beach, Fla.)* 30.22 (2018), e1705590. DOI: 10.1002/adma.201705590.

[2] Ariel Rosenman et al. “Review on Li–Sulfur Battery Systems: an Integral Perspective”. In: *Advanced Energy Materials* 5.16 (2015). ISSN: 1614-6832. DOI: 10.1002/aenm.201500212.

[3] Meng Zhao et al. “A Perspective toward Practical Lithium-Sulfur Batteries”. In: *ACS central science* 6.7 (2020), pp. 1095–1104. ISSN: 2374-7943. DOI: 10.1021/acscentsci.0c00449.

[4] E. Peled et al. “Improving the Durability and Minimizing the Polysulfide Shuttle in the Li/S Battery”. In: *Journal of The Electrochemical Society* 165.1 (Nov. 2017), A6051. DOI: 10.1149/2.0101801jes. URL: https://dx.doi.org/10.1149/2.0101801jes.

[5] Grace Whang and Wolfgang G. Zeier. “Transition Metal Sulfide Conversion: A Promising Approach to Solid-State Batteries”. In: *ACS Energy Letters* 8.12 (2023), pp. 5264–5274. ISSN: 2380-8195. DOI: 10.1021/acsenergylett.3c02246.

[6] T. B. Kim et al. “Electrochemical properties of sodium/pyrite battery at room temperature”. In: *Journal of Power Sources* 174.2 (2007), pp. 1275–1278. ISSN: 03787753. DOI: 10.1016/j.jpowsour.2007.06.093.

[7] Jordi Cabana et al. “Beyond intercalation-based Li-ion batteries: the state of the art and challenges of electrode materials reacting through conversion reactions”. In: *Advanced materials (Deerfield Beach, Fla.)* 22.35 (2010), E170–92. DOI: 10.1002/adma.201000717.

[8] Xiaojie Bai et al. “Pyrite–Based Solid–State Batteries: Progresses, Challenges, and Perspectives”. In: *Advanced Functional Materials* 35.10 (2025). ISSN: 1616-301X. DOI: 10.1002/adfm.202416808.

[9] T. A. Yersak. “Solid-State Electode Engineering and Material Processing for All-Solid-State Lithium and Lithium-Ion Batteries”. PhD thesis. University of Colorado, Boulder, 2012.

[10] Yuping Liu et al. “Recent Advances in Transition–Metal–Based Catalytic Material for Room–Temperature Sodium–Sulfur Batteries”. In: *Advanced Functional Materials* 34.5 (2024). ISSN: 1616-301X. DOI: 10.1002/adfm.202302626.

[11] Jürgen Janek and Wolfgang G. Zeier. “A solid future for battery development”. In: *Nature Energy* 1.9 (2016). DOI: 10.1038/nenergy.2016.141.

[12] Jung Tae Kim et al. “All-solid-state lithium–sulfur batteries through a reaction engineering lens”. In: *Nature Chemical Engineering* 1.6 (2024), pp. 400–410. DOI: 10.1038/s44286-024-00079-5.

[13] Jürgen Janek and Wolfgang G. Zeier. “Challenges in speeding up solid-state battery development”. In: *Nature Energy* 8.3 (2023), pp. 230–240. DOI: 10.1038/s41560-023-01208-9.

[14] Saneyuki Ohno and Wolfgang G. Zeier. “Toward Practical Solid-State Lithium–Sulfur Batteries: Challenges and Perspectives”. In: *Accounts of Materials Research* 2.10 (2021), pp. 869–880. ISSN: 2643-6728. DOI: 10.1021/accountsmr.1c00116.

[15] Samuel Carrara et al. *Supply chain analysis and material demand forecast in strategic technologies and sectors in the EU: A foresight study.* Luxembourg, 2023. DOI: 10.2760/386650. URL: https://op.europa.eu/o/opportal-service/download-handler?identifier=9e17a3c2-c48f-11ed-a05c-01aa75ed71a1&format=pdf&language=en&productionSystem=cellar&part=.

[16] Claude Delmas. “Sodium and Sodium–Ion Batteries: 50 Years of Research”. In: *Advanced Energy Materials* 8.17 (2018). ISSN: 1614-6832. DOI: 10.1002/aenm.201703137.

[17] Prasant Kumar Nayak et al. “From Lithium-Ion to Sodium-Ion Batteries: Advantages, Challenges, and Surprises”. In: *Angewandte Chemie (International ed. in English)* 57.1 (2018), pp. 102–120. DOI: 10.1002/anie.201703772.

[18] Micha P. Fertig et al. “From High– to Low–Temperature: The Revival of Sodium–Beta Alumina for Sodium Solid–State Batteries”. In: *Batteries & Supercaps* 5.1 (2022). ISSN: 2566-6223. DOI: 10.1002/batt.202100131.

[19] Hayley S. Hirsh et al. “Sodium–Ion Batteries Paving the Way for Grid Energy Storage”. In: *Advanced Energy Materials* 10.32 (2020). ISSN: 1614-6832. DOI: 10.1002/aenm.202001274.

[20] Robert Usiskin et al. “Fundamentals, status and promise of sodium-based batteries”. In: *Nature Reviews Materials* 6.11 (2021), pp. 1020–1035. ISSN: 2058-8437. DOI: 10.1038/s41578-021-00324-w.

[21] Jingkang Ma et al. “Toward the Advanced Next–Generation Solid–State Na–S Batteries: Progress and Prospects”. In: *Advanced Functional Materials* 33.20 (2023). ISSN: 1616-301X. DOI: 10.1002/adfm.202214430.

[22] Hui-Ling Yang et al. “Progress and Challenges for All–Solid–State Sodium Batteries”. In: *Advanced Energy and Sustainability Research* 2.2 (2021). ISSN: 2699-9412. DOI: 10.1002/aesr.202000057.

[23] Grayson Deysher et al. “Evaluating Electrolyte-Anode Interface Stability in Sodium All-Solid-State Batteries”. In: *ACS applied materials & interfaces* 14.42 (2022), pp. 47706–47715. DOI: 10.1021/acsami.2c12759.

[24] Jian–Fang Wu et al. “Inorganic Solid Electrolytes for All–Solid–State Sodium Batteries: Fundamentals and Strategies for Battery Optimization”. In: *Advanced Functional Materials* 31.13 (2021). ISSN: 1616-301X. DOI: 10.1002/adfm.202008165.

[25] Meng Wu et al. “Structure designing, interface engineering, and application prospects for sodium–ion inorganic solid electrolytes”. In: *InfoMat* 6.9 (2024). ISSN: 2567-3165. DOI: 10.1002/inf2.12606.

[26] Lin Li et al. “Thermal-Induced Cathodic Interface Change on Na 3 PS 4 -Based All-Solid-State Sodium Batteries”. In: *Industrial & Engineering Chemistry Research* 63.17 (2024), pp. 7699–7707. ISSN: 0888-5885. DOI: 10.1021/acs.iecr.4c00901.

[27] Yayuan Liu, Yangying Zhu, and Yi Cui. “Challenges and opportunities towards fast-charging battery materials”. In: *Nature Energy* 4.7 (2019), pp. 540–550. DOI: 10.1038/s41560-019-0405-3.

[28] Huimin Song et al. “All-solid-state Li-S batteries with fast solid-solid sulfur reaction”. In: *Nature* 637.8047 (2025), pp. 846–853. DOI: 10.1038/s41586-024-08298-9.

[29] Xuming Yang and Andrey L. Rogach. “Electrochemical Techniques in Battery Research: A Tutorial for Nonelectrochemists”. In: *Advanced Energy Materials* 9.25 (2019). ISSN: 1614-6832. DOI: 10.1002/aenm.201900747.

[30] D. Linden T. B. Reddy. *Hanbook of Batteries*. McGraw-Hill, Third Edition, New York, 2002.

[31] Richard Treptow. “Lithium Batteries: A Practical Application of Chemical Principles”. In: *Journal of Chemical Education - J CHEM EDUC* 80 (Sept. 2003). DOI: 10.1021/ed080p1015.

[32] Johannes Kasnatscheew et al. “A Tutorial into Practical Capacity and Mass Balancing of Lithium Ion Batteries”. In: *Journal of The Electrochemical Society* 164.12 (2017), A2479–A2486. ISSN: 0013-4651. DOI: 10.1149/2.0961712jes.

[33] Ossila. *What is a Battery C-Rate? Definition and Calculations*. Consultato il 23 agosto 2025. 2025. URL: https://www.ossila.com/pages/what-is-battery-c-rate.

[34] Allen J. Bard and Larry R. Faulkner. *Electrochemical Methods: Fundamentals and Applications*. 2nd. Wiley, 2001.

[35] Xia Huang et al. "Cyclic Voltammetry in Lithium–Sulfur Batteries—Challenges and Opportunities". In: *Energy Technology* 7.8 (2019). ISSN: 2194-4288. DOI: 10.1002/ente.201801001.

[36] Yihan Xiao et al. "Understanding interface stability in solid-state batteries". In: *Nature Reviews Materials* 5.2 (2020), pp. 105–126. DOI: 10.1038/s41578-019-0157-5.

[37] Gökhan Yüksek and Alkan Alkaya. "Effect of the Depth of Discharge and C-Rate on Battery Degradation and Cycle Life". In: *2023 14th International Conference on Electrical and Electronics Engineering (ELECO)*. IEEE, 2023, pp. 1–5. ISBN: 979-8-3503-6049-3. DOI: 10.1109/ELECO60389.2023.10415967.

[38] Lithium Inventory. *Principles of Electrochemical Impedance Spectroscopy (EIS)*. Accessed: 2025-03-22. 2025. URL: https://lithiuminventory.com/experimental-electrochemistry/eis/principles/.

[39] Dafaalla M.D. Babiker et al. "Recent progress of composite polyethylene separators for lithium/sodium batteries". In: *Journal of Power Sources* 564 (2023), p. 232853. ISSN: 0378-7753. DOI: 10.1016/j.jpowsour.2023.232853.

[40] Saneyuki Ohno et al. "Linking Solid Electrolyte Degradation to Charge Carrier Transport in the Thiophosphate-Based Composite Cathode toward Solid-State Lithium-Sulfur Batteries". In: *Advanced Functional Materials* 31 (Feb. 2021). DOI: 10.1002/adfm.202010620.

[41] *Electronic conductivity measurement using DC and AC method*.

[42] N. D. Mermin N. W. Ashcroft. *Solid State Physics*. Hartcourt College Publishers, 1976.

[43] Encyclopaedia Britannica. *Bragg's Law*. Accessed: 7-Feb-2025. 2024. URL: https://www.britannica.com/science/Bragg-law.

[44] G. Hübschen I. Altpeter R. Tschuncky H. Herrmann. *Materials Characterization Using Nondestructive Evaluation (NDE) Methods*. Woodhead Publishing, 2016.

[45] J.I. Goldstein D.E. Newbury P. Echlin D.C. Joy C.E. Lyman E. Lifshin L. Sawyer J.R: Michael. *Scanning Electron Microscopy and X-Ray Microanalysis, third ediдtion*. Springer Science+Business Media, New York, 2003.

[46] Nguyen A. Farmani P.K. Singh B. Han V.K. Tomer T.A. *Nanosensor for Smart Cities*. Elsevier, 2020.

[47] Thermo Fisher Scientific. *EDS Technology Overview*. Accessed: 7-Feb-2025. 2024. URL: https://www.thermofisher.com/de/de/home/materials-science/eds-technology.html.

[48] G. Greczynski and L. Hultman. "X-ray photoelectron spectroscopy: Towards reliable binding energy referencing". In: *Progress in Materials Science* 107 (2020), p. 100591. ISSN: 00796425. DOI: 10.1016/j.pmatsci.2019.100591.

[49] Vaithiyalingam Shutthanandan et al. "Applications of XPS in the characterization of Battery materials". In: *Journal of Electron Spectroscopy and Related Phenomena* 231 (2019), pp. 2–10. ISSN: 03682048. DOI: 10.1016/j.elspec.2018.05.005.

[50] John F. Moulder et al. *Handbook of X-ray Photoelectron Spectroscopy*. Physical Electronics, Inc., 1995.

[51] Fred A. Stevie and Carrie L. Donley. "Introduction to x-ray photoelectron spectroscopy". In: *Journal of Vacuum Science & Technology A: Vacuum, Surfaces, and Films* 38.6 (2020). ISSN: 0734-2101. DOI: 10.1116/6.0000412.

[52] Sebastian Wenzel et al. "Interfacial Reactivity Benchmarking of the Sodium Ion Conductors Na3PS4 and Sodium b-Alumina for Protected Sodium Metal Anodes and Sodium All-Solid-State Batteries". In: *ACS*

applied materials & interfaces 8.41 (2016), pp. 28216–28224. DOI: 10.1021/acsami.6b10119.

[53] Jia Zhang and Tianye Zheng. "Group IVA Alloy Anodes for Sodium–Ion Rechargeable Batteries: Electrochemistry, Mechanics, and Kinetics". In: *Batteries & Supercaps* (2025). ISSN: 2566-6223. DOI: 10.1002/batt.202400823.

[54] L. D. Ellis, T. D. Hatchard, and M. N. Obrovac. "Reversible Insertion of Sodium in Tin". In: *Journal of The Electrochemical Society* 159.11 (2012), A1801–A1805. ISSN: 0013-4651. DOI: 10.1149/2.037211jes.

[55] Yi Yuan et al. "Self-sacrifice of sulfide electrolytes facilitating stable solid-state sodium–sulfur batteries". In: *Energy & Environmental Science* 18.9 (2025), pp. 4288–4301. ISSN: 1754-5692. DOI: 10.1039/D4EE06171C.

[56] Laura E. Goodwin et al. "Protective NaSICON Interlayer between a Sodium-Tin Alloy Anode and Sulfide-Based Solid Electrolytes for All-Solid-State Sodium Batteries". In: *ACS applied materials & interfaces* 15.43 (2023), pp. 50457–50468. DOI: 10.1021/acsami.3c09256.

[57] W. Volk K.;Mueller. "Zeitschrift fuer Naturforschung, Teil B. Anorganische Chemie". In: *Organische Chemie (2,1947-32,1977), 33, 275 - 278* (1978).

[58] Chengwei Wang et al. "In Situ Neutron Depth Profiling of Lithium Metal-Garnet Interfaces for Solid State Batteries". In: *Journal of the American Chemical Society* 139.40 (2017), pp. 14257–14264. DOI: 10.1021/jacs.7b07904.

[59] Changhong Wang et al. "Identifying soft breakdown in all-solid-state lithium battery". In: *Joule* 6.8 (2022), pp. 1770–1781. ISSN: 2542-4351. DOI: 10.1016/j.joule.2022.05.020.

[60] Matilde Pavan et al. "Role and Evolution of FeS 2 Cathode Microstructure in Argyrodite-Based All-Solid-State Lithium–Sulfur Bat-

teries". In: *Chemistry of Materials* 37.9 (2025), pp. 3185–3196. ISSN: 0897-4756. DOI: 10.1021/acs.chemmater.4c03315.

[61] Philip Minnmann et al. "Editors' Choice—Quantifying the Impact of Charge Transport Bottlenecks in Composite Cathodes of All-Solid-State Batteries". In: *Journal of The Electrochemical Society* 168.4 (Apr. 2021), p. 040537. DOI: 10.1149/1945-7111/abf8d7. URL: https://dx.doi.org/10.1149/1945-7111/abf8d7.

[62] Eva Schlautmann et al. "Impact of the Solid Electrolyte Particle Size Distribution in Sulfide–Based Solid–State Battery Composites". In: *Advanced Energy Materials* 13.41 (2023). ISSN: 1614-6832. DOI: 10.1002/aenm.202302309.

[63] Xu-Dong Zhang et al. "Structure Design of Cathode Electrodes for Solid–State Batteries: Challenges and Progress". In: *Small Structures* 1.3 (2020). ISSN: 2688-4062. DOI: 10.1002/sstr.202000042.

[64] Felix Schnaubelt et al. "Impurities in Na2S Precursor and their Effect on the Synthesis of W-substituted Na3PS4: Enabling 20 mS cm−1 Thiophosphate Electrolytes for Sodium Solid-State Batteries". unpublished.

[65] *Charge Compensation in X-ray Photoelectron Spectroscopy*. https://www.thermofisher.com/de/de/home/materials-science/learning-center/surface-analysis/charge-compensation.html. Accessed: 3 September 2025.

[66] The MathWorks, Inc. *Lognormal Distribution — MATLAB & Simulink Documentation*. https://www.mathworks.com/help/stats/lognormal-distribution.html. Accessed: 2025-09-12. 2025.

[67] Hongli Wan et al. "Self-Formed Electronic/Ionic Conductive Fe3 S4 @ S @ 0.9Na3 SbS4 ·0.1NaI Composite for High-Performance Room-Temperature All-Solid-State Sodium-Sulfur Battery". In: *Small (Weinheim an der Bergstrasse, Germany)* 16.34 (2020), e2001574. DOI: 10.1002/smll.202001574.

[68] Kaier Shen et al. “Solid Catholyte with Regulated Interphase Redox for All-Solid-State Lithium-Sulfur Batteries”. In: *Advanced materials (Deerfield Beach, Fla.)* 37.11 (2025), e2417171. DOI: 10.1002/adma.202417171.

[69] Pushun Lu et al. “Wide-Temperature, Long-Cycling, and High-Loading Pyrite All-Solid-State Batteries Enabled by Argyrodite Thioarsenate Superionic Conductor”. In: *Advanced Functional Materials* 33.8 (2022), pp. 1–16. DOI: 10.1002/adfm.202211211.

[70] Hung Quoc Nguyen et al. “Revealing the Hidden Polysulfides in Solid-State Na-S Batteries: How Pressure and Electrical Transport Control Kinetic Pathways”. In: *Journal of the American Chemical Society* 147.27 (2025), pp. 23492–23503. DOI: 10.1021/jacs.5c00465.

[71] Sanghyeon Kim et al. “High Energy Density CNT/NaI Composite Cathodes for Sodium-Ion Batteries”. In: *Advanced Materials Interfaces* 5.23 (Aug. 2018). DOI: 10.1002/admi.201801342.

[72] Noémie Elgrishi et al. “A Practical Beginner’s Guide to Cyclic Voltammetry”. In: *Journal of Chemical Education* 95.2 (2018), pp. 197–206. ISSN: 0021-9584. DOI: 10.1021/acs.jchemed.7b00361.

[73] G Finch and S Fordham. “The effect of crystal-size on lattice-dimensions”. In: *Proceedings of the Physical Society* 48 (Dec. 2002), p. 85. DOI: 10.1088/0959-5309/48/1/312.

Selbstständigkeitserklärung

Hiermit versichere ich, die vorgelegte Thesis selbstständig und ohne unerlaubte fremde Hilfe und nur mit den Hilfen angefertigt zu haben, die ich in der Thesis angegeben habe. Alle Textstellen, die wörtlich oder sinngemäß aus veröffentlichten Schriften entnommen sind, und alle Angaben die auf mündlichen Auskünften beruhen, sind als solche kenntlich gemacht. Bei den von mir durchgeführten und in der Thesis erwähnten Untersuchungen habe ich die Grundsätze gute wissenschaftlicher Praxis, wie sie in der ‚Satzung der Justus Liebig-Universität zur Sicherung guter wissenschaftlicher Praxis' niedergelegt sind, eingehalten. Entsprechend§ 22Abs. 2der Allgemeinen Bestimmungen für modularisierte Studiengänge dulde ich eine Überprüfung der Thesis mittels Anti-Plagiatssoftware.

Marta Rondo — Giessen, 29/09/25

Signature — Location and Date